Norwegian University
of Life Sciences

Mapping of surface moisture and thermal transmittance of historic building walls with the use of thermography and the heat flow meter method

Karoline Havnes
Structural Engineering and Architecture
Faculty of Science and Technology

Acknowledgments

This master thesis marks the completion of my master's degree in Structural Engineering and Architecture at the Norwegian University of Life Science (NMBU), spring 2019.

Firstly, I would like to express my sincere gratitude towards my supervisor, Thomas Kringlebotn Thiis. I am very grateful for all your patience, experience and guidance throughout the development of this master thesis. I would also like to thank Ingunn Burud for her advises and guidance in programming.

I would also like to express my deepest gratitude to Borgarssysel Museum for letting me preform measurements at Snekkenes.

Finally, I am grateful for all the support and encouragement from my family and friends.

Ås, May 2019

Karoline Havnes

ii

Sammendrag

Historiske bygninger er en unik kilde til kunnskap og erfaringer. Denne type bygninger skiller seg ut i forhold til nåtidens bygninger og huser ofte historiske gjenstander. En forventet endring i det fremtidige klimaet vil medføre endring i innemiljø i de historiske bygningene, hvilket kan ha en negativ påvirkning på mikroklimaet rundt de historiske gjenstander som er bevart i disse bygningene.

En case-studie, av den historiske bygningen Snekkenes på Borgarsyssel Museum i Sarpsborg, ble utført for å kartlegge veggenes overflatefukt og varmegjennomgangskoeffisienten. Disse kartene ble også skapt for å finne områder med høyere risiko for muggvekst og den lineære kuldebroverdi. Overflateforholdene bak de historiske gjenstandene som dekket veggen, presenteres også i denne oppgaven.

Infrarød termografering og varmestrømsmålere ble brukt for å finne varmegjennomgangskoeffisienten til veggene. De termiske bildene fra den infrarøde termograferingen ble også brukt til å lage kart over større deler av veggene, både for varmegjennomgangskoeffisienten og den relative fuktighet på overflaten.

Pix4D ble brukt for å lage kart over temperatur, termisk overføring og relativ fuktighet over overflatene for de større vegginndelingene. Dette programmet ble også brukt for å lage ortofotos fra de visuelle bilder tatt av Snekkenes. De termiske bildene av områder bak de historiske gjenstander ble behandlet i MATLAB, dette fordi kart ikke ble utarbeidet ut fra disse bildene.

Resultatene viste at det var liten eller ingen forskjell mellom varmegjennomgangskoeffisienten beregnet ut ifra de termiske bilder og varmestrømsmålingene på stedet der varmestrømningsmåleren ble plassert i Werenskioldhallen. Innendørs viste imidlertid resultatene at kartene av varmegjennomgangskoeffisienten var sterkt påvirket av konveksjonen innendørs. Utendørs ble det funnet at kartene av varmegjennomgangskoeffisienten var påvirket av endringer i den reflektert temperaturen.

Abstract

Historic buildings are a unique source of knowledge and experiences different from present buildings and often house historical artifacts. An expected change in the future climate is anticipated to change the historical buildings' indoor environment, dangerously affecting the microclimate around the historical artifacts housed in these buildings.

A case study of the historical building Snekkenes at Borgarsyssel Museum, Sarpsborg, was performed in order to map the walls' surface moisture and thermal transmittance. These maps were also generated in order to determine areas at higher risks of mold growth and the linear thermal bridge coefficient. The surface conditions behind the historical artifacts, which covered the wall, are also presented in this thesis.

Infrared thermography and heat flow meters were used in order to determine the thermal transmittance of the walls. The thermal images, from the infrared thermographic survey, were also used in order to generate maps of larger sections of the walls for the thermal transmittance and relative humidity on the surface.

For the larger wall sections, Pix4D was used in order to make maps of the temperature, thermal transmittance and relative humidity over the surfaces. This program was also used in order to generate orthophotos from visual images taken of Snekkenes. The thermal images taken of areas behind the historical artifacts were processed in MATLAB as they were not generated into maps.

The results showed that there was little to no difference between the thermal transmittance calculated from the thermal images and the heat flow meter at the location where the heat flow meter was mounded in Werenskiold-hall. However, in other areas indoor, the resulting thermal transmittance maps were greatly influenced by the indoor convection. Outdoor it was found that the thermal transmittance maps were affected by changes in the reflected temperature.

Table of content

List of figures

List of tables

Definitions

A	Area [m]
c	The speed of light $(3.00 \cdot 10^8 \; m/s)$
e	The actual water pressure
e_s	The saturated water pressure
E	The emissivity power [kJ]
$E_{\lambda b}$	The spectral blackbody emissive power
E_b	The emissive power of a blackbody
h	Planck's constant $(6.63 \cdot 10^{-34} \; Js)$
h_c	The convective heat transfer coefficients [W/m^{2}K]
h_i	The internal convective heat transfer coefficient [W/m^{2}K]
k	The Boltzmann constant $(1.38 \cdot 10^{-23} J/K)$
Q	The heat rate [W]
q	Heat flux [W/m^2]
RH	The atmosphere relative humidity
RH_s	The relative humidity on the surface
R	The thermal resistance [m^{2}K/W]
R_{si}	The interior surface thermal resistance [m^{2}K/W]
R_{se}	The exterior surface thermal resistance [m^{2}K/W]
T	The temperature [°C] or [K]
T_d	The dew point temperature [°C]
Ti	The indoor atmospheric temperature [°C]
T_{kin}	The real kinetic temperature of an object's surface [°C]
T_o	The outdoor atmospheric temperature [°C]
T_w	The wall's temperature [°C]
U	The thermal transmittance [W/m^{2}K]
v	Wind speed [m/s]
W_{atm}	The radiation from the atmosphere [W/m^2]

W_{obj}	The targeted object's emitted radiation [W/m^2]
W_{refl}	The surrounding radiations reflected of the target object [W/m^2]
W_{tot}	The total radiation [W/m^2]
α	The absorbed radiation
ρ	The reflected radiation
Ψ	The linear thermal transfer coefficient
τ	The transmitted radiation [W/mK]
ε	The emissivity
λ	The wavelength
σ	The Stefan-Boltzmann constant $\left(5.67 \cdot 10^{-8} \frac{W}{m^2\,K^4}\right)$
θ, φ	The direction of emitted radiation

1.Introduction

Historic buildings, such as Snekkenes at Borgarsyssel Museum in Sarpsborg, are a unique source of knowledge and experiences different from present buildings. They contain a unique knowledge about building materials and techniques, as well as stories of how people used to live. These buildings portray practical and esthetic elements important for people from that exact time period. Most of them also house historical artifacts often from the same time period as the building itself, of great historical value. Because of their historical value, many buildings and artifacts are preserved at museums.

Figure 1.1: Images of Snekkenes.

It is expected that future climate changes will affect the preservation of museum collections housed in historical buildings (Huijbregts et al., 2012). The effect is expected to be critical as changes of the historical buildings indoor environment will affect the microclimate around the historical artifacts housed in these buildings' (Huijbregts et al., 2012). Changes in the microclimate may result in damaged historical artifacts (Huijbregts et al., 2012), which is not a preferred outcome for the museums. As the first barrier between the indoor and outdoor climate is the building itself, the extent of the outdoor climate's influence on the indoor climate is determined by the building envelope (Ankersmit & Stappers, 2017).

A common method, in order to analyze the thermal behavior of a building envelope, is infrared thermography (Natephra et al., 2017). It is a widely used method, in order to detect faults in building materials influenced by e.g. thermal bridges and moisture, which are deficiencies in the building envelopes (Garrido et al., 2018; Natephra et al., 2017). As this method is non-destructive (Bienvenido-Huertas et al., 2019), it is favorable to use on historical buildings as destructive methods are not possible to carry out because of the buildings' historical value (Nardi et al., 2014).

The use of infrared thermography, or IRT, is currently a highly researched method for calculating the thermal transmittance of building elements (Bienvenido-Huertas et al., 2019). The use of heat flow meter (HFM), normalized by ISO 9869, is one approach used in order to

determine the thermal transmittance of a building element (Nardi et al., 2014). This method, however, only gives a punctual value of the building element's thermal transmittance (Nardi et al., 2014). In order to determine other areas, another measurement campaign is necessary (Nardi et al., 2014).

1.1 Aim of thesis

The main aim of this thesis is to map the moisture and thermal transmittance of the walls of a historic building with the use of thermography and heat flow meter.

The key questions for this thesis to answer will be, based on the mapping of moisture and thermal properties:

1. Which areas have a higher risk of mold growth?
2. What are the surface conditions behind the historical artifacts covering the walls?
3. What are the walls' thermal transmittance and what are the differences between indoor and outdoor mapping of thermal transmittance?
4. Will the computed mapping of thermal transmittance give reliable results in order to calculate the linear thermal bridge coefficient?

These questions will be answered based on a case study of Snekkenes at Borgarsyssel Museum.

2. Theory

The theoretical foundation, which the following thesis is built upon, is presented in the present chapter. Firstly, the concept of humidity, surface moisture and mold growth, section 2.1. Secondly, the concepts concerning heat transfer, the thermal transmittance found with thermography and heat flow meters, and thermal bridges, section 2.2. Section 2.3, present the concepts related to photogrammetry.

2.1 Humidity

Humidity is air that consists of a certain quantity of moisture in the form of water vapor (Edvardsen & Ramstad, 2014a). To indicate the quantity of moisture in the atmosphere, relative humidity is most commonly used (Edvardsen & Ramstad, 2014a). Relative humidity, or RH, is the ratio between the water vapor pressure in the atmosphere and the saturated water vapor pressure (Edvardsen & Ramstad, 2014a) . The equation for relative humidity is written as

$$\text{RH} = 100 \left(\frac{e}{e_s}\right) \tag{2.1}$$

where e is the water vapor pressure and e_s is the saturated water pressure (Edvardsen & Ramstad, 2014a). When the water vapor pressure is saturated, it means that the gas phase is in equilibrium with the liquid phase or the solid phase at a given temperature (Edvardsen & Ramstad, 2014a; *Metningstrykk*, 2009). The temperature, at the saturated water pressure, is known as the dew point temperature (Edvardsen & Ramstad, 2014a).

2.1.1 Dew point temperature

Temperatures greatly affect humidity as the temperature sets an upper limit of how much water vapor the atmosphere is capable of containing (Edvardsen & Ramstad, 2014a). The temperature at the upper limit is known as the dew point temperature and is where the water vapor pressure is saturated (Edvardsen & Ramstad, 2014a). An increase in the atmospheric temperature will also result in an increase in the amount of water vapors the atmosphere can contain, as well as a higher dew point temperature (Edvardsen & Ramstad, 2014a). Lower temperatures, however, will have the opposite effect. At lower temperatures, below the dew point temperature, excessive water vapor will condense on surfaces or become droplets in the air (Edvardsen & Ramstad, 2014a). This is because the atmosphere cannot contain any more water as the relative humidity is at 100% (Edvardsen & Ramstad, 2014a). The dew point temperature, T_d, can be

defined as the temperature to which the atmosphere must be cooled, in an isobaric process, in order to become saturated (Lawrence, 2005; Monteith & Unsworth, 2013), see equation (2.2).

$$e_s(T_d) = e(T_{atm})$$ (2.2)

An expression for the saturated water pressure, dependent on the temperature, T_{atm}, is necessary to express the dew point temperature in terms of relative humidity (Lawrence, 2005). Equation (2.3), known as the August-Roche-Magnus formula, is a highly accurate empirical expression of this (Lawrence, 2005).

$$e_s = C * \exp\left(\frac{A \cdot T_{atm}}{B + T_{atm}}\right)$$ (2.3)

The recommended coefficient values are as follows: $A = 17.67$, $B = 243.5$, and $C = 6.112$ (Bolton, 1980; Thiis et al., 2017).

The dew point temperature can be expressed as a function of the ambient vapor pressure and temperature by substituting equation (2.3) in equation (2.2) (Lawrence, 2005), which gives

$$T_d = \frac{B \cdot \ln\left(\frac{e}{C}\right)}{A - \ln\left(\frac{e}{C}\right)}$$ (2.4)

Combining equation (2.4) with equation (2.1) gives (Lawrence, 2005)

$$T_d = \frac{B \left[\ln\left(\frac{RH}{100}\right) + \frac{A \cdot T_{atm}}{B + T_{atm}}\right]}{A - \ln\left(\frac{RH}{100}\right) - \frac{A \cdot T_{atm}}{B + T_{atm}}}$$ (2.5)

2.1.2 Relative humidity on surface

Even if the atmospheric temperature is higher than the dew point temperature, this might not be the case for surface temperatures (Gustavsen et al., 2008). For example, walls and furniture may have a lower temperature than the temperature in the atmosphere (Gustavsen et al., 2008). Low surface temperature and high humidity often result in surface moisture (Gustavsen et al., 2008). The surface temperature must be lower than the dew point temperature, resulting in moisture occurring on the surface (Gustavsen et al., 2008). By combining equation (2.1), (2.2), and (2.3), the relative humidity on the surface, RH_s, can be expressed as

$$RH_s = 100 \frac{exp\left(\frac{A \cdot T_d}{B + T_d}\right)}{exp\left(\frac{A \cdot T_s}{B + T_s}\right)} \quad\quad (2.6)$$

where T_s [°C] is the surface temperature (Thiis et al., 2017).

2.1.3 Mold

Surface moisture, as well as high levels of relative humidity, should be prevented as it may result in mold growth (Gustavsen et al., 2008). Mold can be both esthetic unappealing and destructive and is a normal occurrence in all environments (Folkehelseinstituttet, 2013; Gustavsen et al., 2008). There are, however, great variations in the occurrence of mold spores with the seasons (Folkehelseinstituttet, 2013). In the outdoor atmosphere, during summer and autumn, is when the highest number of spores are found, for most types (Folkehelseinstituttet, 2013). In these seasons, the outdoor atmosphere is the main source of mold, also indoor (Folkehelseinstituttet, 2013).

Time, nutrition, temperature and water/moisture are the four conditions necessary for mold to grow (Holme & Geving). Dead organic materials are the molds source of energy and nutrition that it needs to grow (Holme & Geving). The temperature is also an important factor for mold to grow (Holme & Geving). A temperature around 25 – 30°C is optimal for most species, but many also thrive with lower temperatures (Holme & Geving). At temperatures near zero, mold growth stagnates and the mold species that hibernate often survive being frozen (Holme & Geving). The mold growth also stagnates at temperatures exceeding 25 – 30°C and most species die when the temperature reaches 40 – 50°C (Holme & Geving).

There is variation between the humidity required for the different type of mold species to thrive (Holme & Geving). A relative humidity on the surface, or in the pores, over 80 – 85% is necessary for most mold species to grow (Holme & Geving). It is, however, important to note that there is no universal safe, risk-free relative humidity for all materials (Ankersmit & Stappers, 2017). The only generalization possible is that a relative humidity above 75 % over long periods are dangerous (Ankersmit & Stappers, 2017). There is also an increase in growth speed as the relative humidity reaches 100 %, as well as more species thriving at higher levels of relative humidity (Holme & Geving). Mold may also grow at low levels of humidity because of nutrition such as dirt or dust (Folkehelseinstituttet, 2013).

2.2 Heat transfer

Heat, a form of energy, is transferred from an area with higher temperatures to an area with lower temperatures, which also applies through structures (Edvardsen & Ramstad, 2014b). There are three forms of heat transfer, or thermal transfer:

- Conduction: Conduction is the transport of energy through physical contact. This type of thermal transfer is a result of molecules with high levels of fluctuation colliding with molecules with less motion energy (Edvardsen & Ramstad, 2014b). In the collision, kinetic energy is transferred from the strongly fluctuating molecule over to the slower molecule (Edvardsen & Ramstad, 2014b).
- Convection: Convection is thermal transfer by moving air or fluids (Edvardsen & Ramstad, 2014b).
- Radiation: Thermal radiation is invisible to the naked eye, but consists of infrared waves emitted from objects with a temperature above absolute zero (Butcher, 2016).

Though there are three types of thermal transfer, a medium may only involve two of them simultaneously, see figure 2.1 (Çengel et al., 2015). The thermal transfer through a medium can be used in order to determine thermal transmittance, or U-value, of a building element (Çengel et al., 2015; Edvardsen & Ramstad, 2014b).
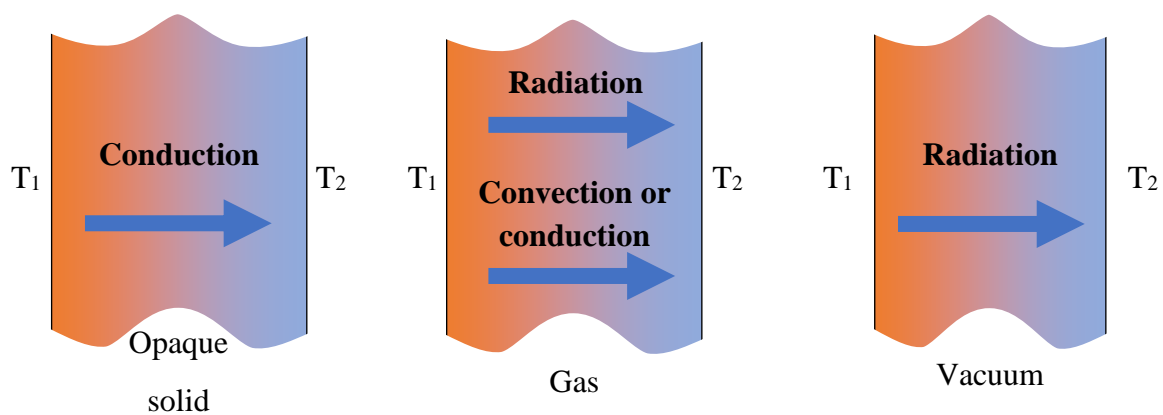
Figure 2.1: The three forms of thermal transfer, where $T_1 > T_2$. Modified figure from (Çengel et al., 2015)

2.2.1 Infrared thermography

The use of infrared thermography, or IRT, is currently a highly researched method for calculating the thermal transmittance of building elements (Bienvenido-Huertas et al., 2019). The infrared camera records the total thermal radiation emitted from an area or an object and converts the information into a visual image of the temperature conditions (*Termografi: avbilding*, 2018). The image is created by assigning a color to each temperature, resulting in a false-color image known as a thermogram (Usamentiaga et al., 2014). From the records by the camera, it is possible to distinguish temperature differences of as little as a fraction of one degree (*Termografi: avbilding*, 2018).

2.2.1.1 The principles of infrared thermography

The use of infrared thermography is a non-destructive, remote, sensitive method used to capture the infrared waves (*Termografi: avbilding*, 2018). Infrared waves are a form of electromagnetic radiation with longer wavelengths than visible light, and are therefore invisible to the naked eye (Butcher, 2016). Though invisible, all objects with a temperature above absolute zero emit infrared waves (Butcher, 2016; *Termografi: avbilding*, 2018). As mentioned earlier, this is known as the thermal radiation. Unlike conduction and convection, the radiation energy is transferred without the use of a medium (Kuenzer & Dech, 2013).

In order to determine the thermal radiation of an object, it is necessary to introduce the theory of a blackbody, or a perfect black body. A perfect black body is nonexistent, but is an ideal emitter and absorber of radiation (Kuenzer & Dech, 2013). Objects with such surfaces therefore emit the maximum possible amount of energy at a certain wavelength and temperature (Kuenzer & Dech, 2013; Usamentiaga et al., 2014). At a given wavelength, λ, the spectral blackbody emissive power, $E_{\lambda b}$, can be calculated as a function of the blackbody's absolute temperature (Çengel et al., 2015; Kuenzer & Dech, 2013; Usamentiaga et al., 2014). This is known as Planck's Law (Kuenzer & Dech, 2013; Usamentiaga et al., 2014)

$$E_{\lambda b}(T)d\lambda = \frac{2 \cdot \pi \cdot h \cdot c^2}{\lambda^5 (exp(\frac{h \cdot c}{\lambda \cdot k \cdot T}) - 1)} d\lambda \tag{2.7}$$

where h is the Planck's constant ($6.63 \cdot 10^{-34} \, Js$), c is the speed of light ($3.00 \cdot 10^8 \, m/s$), and k is the Boltzmann constant ($1.38 \cdot 10^{-23} J/K$) (Kuenzer & Dech, 2013; Vollmer & Möllmann, 2011).

The emissive power of a blackbody, E_b, for a whole spectrum can be calculated by integrating Planck's law from zero to infinity (Usamentiaga et al., 2014), see equation (2.8) .

$$E_b(T) = \int_0^\infty E_\lambda(T)d\lambda = \sigma \cdot T^4 \tag{2.8}$$

This is known as the Stefan-Boltzmann formula, where σ is Stefan-Boltzmann constant $\left(5.67 \cdot 10^{-8} \frac{W}{m^2 \, K^4}\right)$ (Kuenzer & Dech, 2013; Usamentiaga et al., 2014).

As mentioned, a surface with a perfect black body is nonexistent. The real emitted radiation of a surface is therefore given by scaling the radiation of a perfect black body by a factor ε, known as emissivity (Vollmer & Möllmann, 2011). The emissivity is defined as an object's capability of emitting thermal radiation compared to that of a perfect black body at the same temperature (*emissivitet*, 2018). Therefore, emissivity has a range of $0 \leq \varepsilon \leq 1$ (Vollmer & Möllmann, 2011).

A real surface emissivity is not constant, but differ at different surface temperatures as well as changes in the direction and wavelength of the emitted radiation (Çengel et al., 2015). The emissivity, at a given temperature, can therefore be written as a function of wavelength, the

emitted radiation's direction and the surface temperature (Çengel et al., 2015), see equation (2.9).

$$\varepsilon(\lambda, \theta, \varphi, T) = \frac{E(\lambda, \theta, \varphi, T)}{E_b(\lambda, T)}$$ (2.9)

Here, $E(\lambda, \theta, \varphi, T)$ is the emissive power of the real surface, λ is the specified wavelength of the radiation emitted by the real surface and blackbody, θ and φ are the directions of the emitted radiation and T is the temperature of the real surface and the blackbody (Çengel et al., 2015).

As a result of the complexity that arises due to the wavelength and direction of the emissivity, the diffuse and gray approximations are often utilized in order to calculate the emissivity (Çengel et al., 2015). Thus, the emissivity becomes a constant value at a given temperature as the properties of a diffuse surface is independent of wavelength and a gray surface is independent of direction (Çengel et al., 2015). Thnae resulting emissivity is known as the total hemispherical emissivity and is acquired by averaging over all wavelengths and directions (Çengel et al., 2015), see equation (2.10). Table 2.1 contain different material's surface emissivity at certain temperatures.

$$\varepsilon(T) = \frac{E(T)}{E_b(T)}$$ (2.10)

Table 2.1: Surface emissivity of different materials at 300 K (Çengel et al., 2015).

Material	Emissivity, ε
Aluminum foil	0.07
Window glass	0.90 – 0.95
Oil paints of all colors	0.92 – 0.96
Black paint	0.98

The present thesis is also founded on another approximation, which is that the radiation is considered as a surface phenomenon for materials that are opaque to thermal radiation, e.g. wood, rocks and metal (Çengel et al., 2015). This means that the radiation is emitted and absorbed within a few microns from the surface (Çengel et al., 2015). Opaque materials can also be described as materials that do not transmit radiation (Çengel et al., 2015).

Due to the conservation of energy, the first law of thermodynamics, the incident radiation on the surface can either be absorbed, α, reflected, ρ, or transmitted, τ (Çengel et al., 2015), see equation (2.11).

$$\alpha + \rho + \tau = 1 \tag{2.11}$$

As the fraction of radiation that is transmitted, τ, is considered to be zero for opaque materials, equation (2.11) can be rewritten as equation (2.12) (Çengel et al., 2015).

$$\alpha + \rho = 1 \tag{2.12}$$

Kirchhoff's law of radiation states that at a given temperature and wavelength, the emissivity and absorption of a surface are equal, which can be written as (Usamentiaga et al., 2014)

$$\alpha = \varepsilon \tag{2.13}$$

From equation (2.12) and (2.13), equation (2.14) is obtained for opaque materials (Usamentiaga et al., 2014).

$$\varepsilon + \rho = 1 \tag{2.14}$$

2.2.1.2 *The atmospheric effects*

As thermography is a remote sensing method, other sources of radiation affect the thermal readings to different degrees. In order to retrieve the correct kinetic temperature of the object, the theoretical background of thermal radiation described in section 2.2.1.1 is used. There are three sources of radiation that affect the total radiation, W_{tot}, captured by the infrared camera (Usamentiaga et al., 2014). This can be expressed as

$$W_{tot} = W_{obj} + W_{refl} + W_{atm} \tag{2.15}$$

where W_{obj} is the targeted object's emitted radiation, W_{refl} is the surrounding, or background, radiations reflected of the target object, and W_{atm} is the radiation from the atmosphere (Usamentiaga et al., 2014). With the use of Stefan-Boltzmann's law, the three sources radiation may be expressed in the following way (Usamentiaga et al., 2014)

$$W_{obj} = \varepsilon_{obj} \cdot \tau_{atm} \cdot \sigma \cdot \left(T_{obj}\right)^4 \tag{2.16}$$

$$W_{ref} = \rho_{obj} \cdot \tau_{atm} \cdot \sigma \cdot \left(T_{ref}\right)^4 \tag{2.17}$$

$$W_{atm} = \varepsilon_{atm} \cdot \sigma \cdot \left(T_{atm}\right)^4 \tag{2.18}$$

Here, ε_{obj} is the object's emissivity, τ_{atm} is the atmosphere's transmittance, T_{obj} is the object's temperature, ρ_{obj} is the object's reflectivity, T_{ref} is the reflected temperature, ε_{atm} is the emissivity of the atmosphere, and T_{atm} is the atmosphere's temperature (Usamentiaga et al., 2014). Equation (2.17) can be re-written with the use of equation (2.14), resulting in equation (2.19) (Usamentiaga et al., 2014). With the use of equation (2.11) and assuming $\rho_{atm} = 0$, equation (2.18) can be re-written into equation (2.20) (Usamentiaga et al., 2014).

$$W_{ref} = \left(1 - \varepsilon_{obj}\right) \cdot \tau_{atm} \cdot \sigma \cdot \left(T_{ref}\right)^4 \tag{2.19}$$

$$W_{atm} = (1 - \tau_{atm}) \cdot \sigma \cdot (T_{atm})^4 \tag{2.20}$$

Equation (2.15) can then be rewritten and solved for the object's temperature as follows

$$T_{obj} = \sqrt[4]{\frac{(W_{tot}) - \left(1 - \varepsilon_{obj}\right) \cdot \tau_{atm} \cdot \sigma \cdot \left(T_{ref}\right)^4 - (1 - \tau_{atm}) \cdot \sigma \cdot (T_{atm})^4}{\varepsilon_{obj} \cdot \tau_{atm} \cdot \sigma}} \tag{2.21}$$

The objects emissivity, the reflected temperature, and the atmospheric transmittance and temperature must be applied in order to correct the temperature readings of the object (Usamentiaga et al., 2014). As the atmospheric transmittance is very close to one, as it is estimated from the atmospheric relative humidity and distance to the object, its influence is considered neglectable at fairly small distances (Quang Huy et al., 2017). However, the object's emissivity and the reflected temperature highly influence the thermal readings (Usamentiaga et al., 2014). In most cases, the reflected temperature can be set equal to the atmospheric temperature for objects with high emissivity (Quang Huy et al., 2017).

A correction of the emissivity is in order because real materials have a lower emissivity than 1, as presented in section 2.2.1.1. This means that the real kinetic temperature of an object's surface, T_{kin}, is lower than the radiated temperature, T_{rad} (Kuenzer & Dech, 2013). Based on the Stefan-Boltzmann formula, equation (2.8), and the definition of emissivity, the real kinetic temperature of an object's surface, can be written as (Kuenzer & Dech, 2013)

$$T_{rad} = \varepsilon^{\frac{1}{4}} \cdot T_{kin} \tag{2.22}$$

This indicates that the temperature sensed with the infrared camera, the radiance temperature, can differ significantly even for objects with the same kinetic temperature on the surface [16]. The thermal images must therefore be corrected in order to retrieve the correct kinetic temperature of an object [16]. From the corrected thermal readings, the thermal transmittance may be calculated.

2.2.1.3 *Thermal transmittance of thermal images*

The thermal transmittance, U , can be defined as the "Heat flow rate in the steady state divided by the area and by the temperature difference between the surroundings on each side of the system" (International Organization for Standardization, 2014). This can be written as

$$U = \frac{Q}{(T_i - T_o) \cdot A}$$ (2.23)

where A [m] is the surface area the heat, Q , flows through, T_i is the indoor atmospheric temperature and T_o is the outdoor atmospheric temperature (Madding, 2008).

As a result of conduction in steady state, between the building element and the atmosphere, the thermal transfer can be treated as the sum of the convective, Q_c, and radiative, Q_r, contributions (Bienvenido-Huertas et al., 2019; Madding, 2008). Equation (2.24) can therefore be rewritten as

$$U = \frac{Q_c + Q_r}{(T_i - T_o) \cdot A}$$ (2.24)

Several methods have arisen from equation (2.23) in order to determine the thermal transmittance of building element (Bienvenido-Huertas et al., 2019). Bienvenido-Huertas, D., et al. (Bienvenido-Huertas et al., 2019), analyzed some equations created to determine the thermal transmittance, formulated by different authors, and found there to be little to difference between these equations. Equation (2.25) (Bienvenido-Huertas et al., 2019) was therefore used in order to determine the thermal transmittance of a building element with the use of infrared thermography.

$$U = \frac{h_c(\Delta T_{watm}) + 4\varepsilon\sigma\, T_w^3\left(T_w - T_{ref}\right)}{T_i - T_o}$$ (2.25)

Here, the radiative thermal transfer is given by

$$Q_r = 4 \cdot \varepsilon \cdot \sigma \cdot A \cdot T_w^3(T_w - T_{ref})$$ (2.26)

where ε is the emissivity of the wall, the wall's temperature, T_w, and T_{ref} is the reflected temperature (Bienvenido-Huertas et al., 2019; Madding, 2008). As for the convective thermal transfer, it is given by

$$Q_c = h_c \cdot A \cdot (\Delta T_{watm})$$ (2.27)

where h_c is the convective heat transfer coefficients, and ΔT_{watm} is the temperature difference between the wall surface, T_w, and the atmospheric temperature between the infrared camera and

the object, T_{atm} (Madding, 2008). The convective coefficient is influenced by the air flow conditions, or convection, experienced by the wall (Jayamaha et al., 1996). Commonly, this coefficient is usually estimated with the use of the following correlation

$$h_c = 5.7 + 3.8 \cdot v \tag{2.28}$$

where v is the wind speed (Jayamaha et al., 1996). Based on experimental studies, other correlations have been developed in order to estimate the convective heat transfer coefficient (Jayamaha et al., 1996).

The aim of Bienvenido-Huertas, D., et al. article (Bienvenido-Huertas et al., 2019) was to analyze the internal convective heat transfer coefficient, h_i . Out of the 25 different correlations of temperature differences analyzed by Bienvenido-Huertas, D., et al. (Bienvenido-Huertas et al., 2019), the following internal convective heat transfer coefficient was selected

$$h_i = 3.08(\Delta T_{wi})^{0.25} \tag{2.29}$$

Here, ΔT_{wi} is the absolute temperature difference between the wall surface, T_w, and the indoor atmospheric temperature, T_i (Bienvenido-Huertas et al., 2019).

2.2.2 Thermal resistance and thermal transmittance with the use of the heat flow meter method

Section 2.2.1 describes one of the methods used to calculate the thermal transmittance. Another method, which can be used in order to determine the thermal transmittance, is with the use of the heat flow meter method. The heat flow meter method can be used in order to indicate the total thermal resistance of a building element, which then can be used in order to determine the thermal transmittance of said building element (International Organization for Standardization, 2014).

Thermal resistance, or R-value, is a measurement for thermal transfer or heat loss through a building element (Edvardsen & Ramstad, 2014b). All respective materials in the element consist of a distinctive thermal resistance, which can be summed together in order to achieve the element's total thermal resistance (Edvardsen & Ramstad, 2014b).

If the materials in the building element are unknown, it is possible to measure the total thermal resistance of a building element with the use of the heat flow meter method. The measurements and calculations are to be in accordance with ISO 9869.

According to ISO 9869:2014, the measurements needed, to obtain the thermal resistance, are the surface temperature on both sides of the element as well as the heat flux through the element, (International Organization for Standardization, 2014). It is of importance that the measurements are taken over a sufficiently long period (International Organization for Standardization, 2014). In order to analyze the measurements, ISO 9869:2014 present two

different methods. The average method is a simple method, while the dynamic method is considered more sophisticated (International Organization for Standardization, 2014). For this thesis, the dynamic method will not be further described as it was not used.

With the use of the average method, the thermal resistance can be obtained by dividing the average heat flux by the average temperature difference (International Organization for Standardization, 2014). The average thermal resistance for the period is displayed in equation (2.30) (International Organization for Standardization, 2014).

$$R_{element} = \frac{\sum_{j=1}^{n} (T_{sij} - T_{sej})}{\sum_{j=1}^{n} q_j} \quad (2.30)$$

If the average thermal resistance does not differ by more than 5 %, for three subsequent nights, the measuring period can be concluded (International Organization for Standardization, 2014). Only the data acquired at night, 1 hour after sundown and until sunrise, are recommended for the analysis to avoid the influence of solar radiation (International Organization for Standardization, 2014).

In order to calculate the total thermal resistance, surface layers of air must also be included as they function as a thermal resistance (Çengel et al., 2015; Edvardsen & Ramstad, 2014b). The heat flux through a layer of fluid by convection can be expressed as

$$q_{convection} = h_c \cdot \Delta T \quad (2.31)$$

where ΔT is the temperature difference (Çengel et al., 2015). Another way to define the heat flux is as the heat flow per unit area, equation (2.32) (Çengel et al., 2015).

$$q = \frac{Q}{A} \quad (2.32)$$

As the thermal resistance can be defined as the inverse of the thermal transmittance (Edvardsen & Ramstad, 2014b) the resulting thermal transmittance by combining equation (2.23), (2.31) and (2.32) is

$$R_s = \frac{1}{h_c} \quad (2.33)$$

where R_s is the surface layer's thermal resistance. The total thermal resistance can then be given by

$$R_T = R_{si} + R_{element} + R_{se} \quad (2.34)$$

where R_{si} is the interior surface thermal resistance and R_{se} is the exterior surface thermal resistance (Edvardsen & Ramstad, 2014b). As the thermal resistance was the inverse of the thermal transmittance, the thermal transmittance can be expressed as (Edvardsen & Ramstad, 2014b)

$$U = \frac{1}{R_T} \tag{2.35}$$

A well-insulated element has a low thermal transmittance, while a high value indicates the element is thermally deficient (Edvardsen & Ramstad, 2014b).

2.2.3 Thermal bridges

Thermal bridges are areas of the climate screen, such as walls, where there is a significant change in the thermal resistance (SINTEF Byggforsk, 2008). There are several conditions that can create thermal bridges, such as floor to wall junctions, wall to wall junctions and changes in the materials' thickness, which can lead to numerous unfortunate consequences (SINTEF Byggforsk, 2008). The main consequences are low surface temperatures and an increase in the heat loss (SINTEF Byggforsk, 2008).

Low surface temperatures locally on the inside of structures can be caused by thermal bridges (SINTEF Byggforsk, 2008). The surface temperature depends on the thermal bridge's influence on the structure and the indoor and outdoor temperatures (SINTEF Byggforsk, 2008). Condensation may occur as a result of the low surface temperature caused by the thermal bridges (SINTEF Byggforsk, 2008). The conditions and consequences of low surface temperatures were presented in section 2.1.

The linear thermal bridge can be indicated as the heat loss per unit length of the thermal bridge and per degree temperature difference, known as the linear thermal transfer coefficient, Ψ (SINTEF Byggforsk, 2008). Based on the equation of heat flow, Q, through a construction, equation (2.36), it is possible to estimate the linear thermal transfer coefficient (SINTEF Byggforsk, 1999).

$$Q = U_{TB} \cdot A \cdot (T_i - T_o) = U_o \cdot A \cdot (T_i - T_o) + \Psi \cdot l \cdot (T_i - T_o) \tag{2.36}$$

Here, the U_{TB} is the thermal transmittance of the thermal bridge, U_o is the wall's thermal transmittance in areas without the thermal bridge, A is the areal of the wall, and l is the length of the linear thermal bridge (SINTEF Byggforsk, 1999; SINTEF Byggforsk, 2008). Equation (2.36) can be re-written as

$$\Psi = \frac{(U_c - U) \cdot A}{l} = (U_c - U) \cdot b \tag{2.37}$$

where b is the width of the partition wall or the thickness of the floor junctions (SINTEF Byggforsk, 1999).

2.3 Photogrammetry

The scientific field known as photogrammetry, uses imagery to acquire three-dimensional measurements of objects and surfaces (Kemp, 2008; Thomas et al., 2013). A single image contains insufficient information to perform any three-dimensional mapping, as the two-dimensional image only represent a perspective projection of the three-dimensional world (Kemp, 2008). Overlapping images of the same scene are therefore required for three-dimensional mapping (Kemp, 2008). The necessary overlap depends on the mapping area, but an overlap of at least 60 % is required (Kemp, 2008).

It is possible to determine the coordinates of the photographed object in a three-dimensional space by applying the principle of triangulation using the measurements made in two or more images taken from different angles (Thomas et al., 2013). By reestablishing the geometric situation during exposure, it is possible to derive placement, shape, and size of objects (Andersen, 1981). The geometric properties of the camera are the internal, external, relative and absolute orientation (Andersen, 1981). Successively establishing these parameters correlates with the quality and precision of the products from photogrammetry (Andersen, 1981).

The geometric properties concerning the internal parts of the camera are considered the camera's interior orientation (Andersen, 1981). Focal length, principal points, radial and tangential lens distortion relate to the camera's interior orientation (Andersen, 1981; Thomas et al., 2013).

The camera's spatial rotation and position are the exterior orientation parameters (Andersen, 1981). With these parameters, the camera's projection center may be placed in a three-dimensional space (Andersen, 1981). The position can be defined as a vector; [x, y, z], expressing the camera's projection center position (x, y), and elevation (z) (Andersen, 1981). The camera's rotation is defined as a vector; [ω, φ, κ], where the angles (ω, φ) indicate the direction, and the angle (κ) indicates the rotation around the z-axis (Andersen, 1981).

The relative position and orientation between images relate to the relative orientation (Andersen, 1981). As the images are orientated in relation to each other, the computed model's orientation may not be equivalent with the photographed scenes orientation (Andersen, 1981). An example could be that the model's orientation is upside-down in comparison with the photographed scene. Orientating the model in equivalence with the photographed scene is known as the absolute orientation (Andersen, 1981). The absolute orientation is not needed in order to triangulate the three-dimensional coordinates of the scene in the overlapping images.

2.3.1 Orthophoto

Images are a representation of the reflected rays of light from a scene, in a two-dimensional format (Andersen, 1981). Cameras capture the reflected light by converging it through its projection center and then transfer it onto a two-dimensional plane (Andersen, 1981). A straight line can be drawn from a given point, P, through the project center and back to the initially reflecting object in the three-dimensional world (Andersen, 1981).

As a result of the photo's central projection, stitching images together may create a misrepresentation of the photographed scene (Pix4D). An orthophoto is a photo with map like qualities and is unaffected by the misrepresentation caused by the central projection (Pix4D). The orthophoto consists of an orthogonal projection of the photographed object and has the same scale throughout the product, just like maps (Dick, 2003).
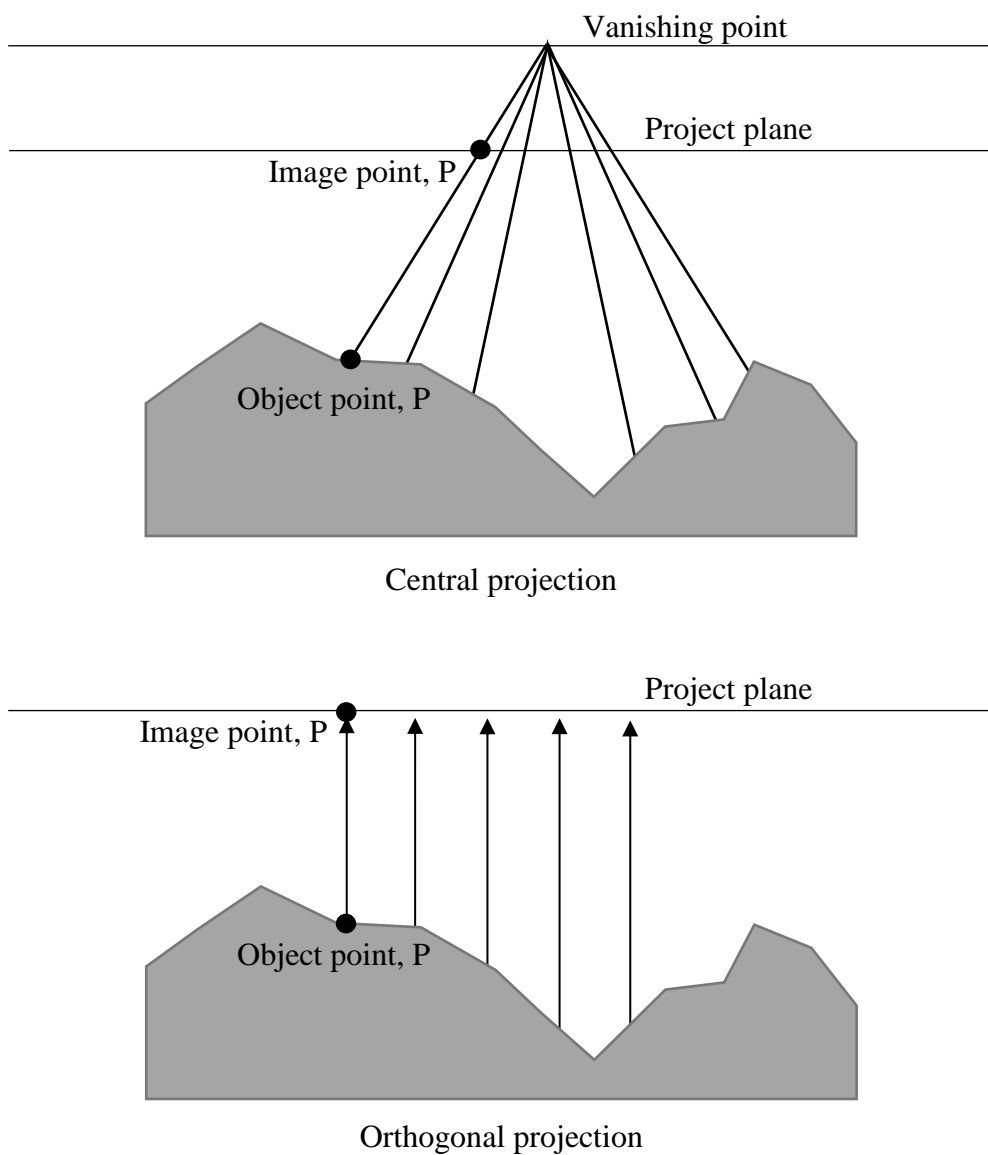
Figure 2.2: Central and Orthogonal projection. Modified figure from (Andersen, 1981).

3. Equipment and software

This chapter presents the main equipment and software used in order to acquire the measurements further described in section 4.2.

3.1 TRSYS01

TRSYS01 is a robust and highly accurate in-situ measuring system for monitoring heat flux and surface temperatures of building elements (Hukseflux). Even with a low temperature difference across the wall, TRSYS01 is assured to continue measuring because of the high accuracy of the sensor measurements (Hukseflux).

The apparatus can measure at two locations at the same time, leading to a high confidence level in the resulting measurements because of the redundancy (Hukseflux). The two locations are provided with one heat flux sensor and a pair of temperature sensors (Hukseflux).

The sensor for measuring heat flux is HFP01, while temperature sensor model, TC, measures the surface temperatures of the different sides of the element (Hukseflux). The uncertainty of the measured temperature difference, between the paired TC-type thermocouple, is better than 0.1 °C and applies over the entire rated temperature range (Hukseflux). Figure 4.5 displays the sensors mounted to a building element.

The right location and conditions are important when installing the sensors. They should not be mounted in areas where they are exposed to e.g. sun, rain, lateral heat fluxes, and drafts (Hukseflux). Thermal bridges and heating devices should also be avoided (Hukseflux). Strongly cooled or heated rooms are ideal, as it results in a constant high level of heat flux (Hukseflux). The difference in temperature must be higher than 10 °C (Bienvenido-Huertas et al., 2019). Additionally, the indoor temperature shall not change by more than 3 °C during the measured period (Hukseflux). More extensive information about the sensor's installation can be found in TRSYS01's user manual.

The measurements from the mounted sensors are stored in the MCU01, which is a measuring system with memory and a clock (Hukseflux). The measurements from the sensors, stored in the MCU, can be downloaded to a computer and be further processed in order to calculate the building element's thermal resistance and thermal transmittance (Hukseflux). In order to determine the thermal resistance and thermal transmittance, the measurements should be used in accordance with ISO 9869 and ASTM C1155/C1046 (Hukseflux).

3.2 Cameras

3.2.1 FLIR T620bx

FLIR T620bx, manufactured by FLIR, is a high-performance infrared camera with the latest technology available (FLIR, 2014). The camera has a field of view of 25° horizontally and 19° vertically as well as a 640 x 480 pixels sized uncooled focal plane array (FLIR, 2014). Technical characteristics of the infrared camera can be consulted in table 3.1.

Table 3.1: FLIR T620bx 25° technical characteristics (FLIR, 2014).

Resolution	640 x 480 pixels
Measurement range	- 40°C to + 150°C + 100°C to + 650°C
Spatial resolution (IFOV)	0.68 mrad
Field of view (FOV)	25° x 19°
Frequency	30 Hz
Accuracy	Max(± 2°C; 2 %) at 25°C nominal

3.2.2 CANON EOS 100D

CANON EOS 100D is a single-lens reflex camera that generates images only representing the reflected visible light of three-dimensional objects. The images can be in the format of JPEG and/or RAW, with a maximum resolution of 5184 x 3456 pixels.

3.3 Pix4D mapper

The image processing software, Pix4D mapper, applies photogrammetry to transform images into digital spatial maps and models (Pix4D, 2017b). The digital images processed in PIX4D can either be in the format of JPEG or TIFF. With TIFF-files, it is possible to use both RGB images as well as thermal images (Pix4D).

3D point clouds and texture models, orthophotos, Digital Surface Model (DSM), and Digital Terrain Models (DTM) are the main outputs of Pix4Dmapper (Pix4D, 2017b). The generated products can be exported to many different formats, making it possible to further process the results in other software such as AutoCAD (Pix4D, 2017b).

There is a desktop version of the software, as well as an opportunity to process the projects in the cloud (Pix4D, 2017b). Images may be directly uploaded to the cloud and processed

automatically (Pix4D, 2017b). In order to define the processing options, the desktop version must be used (Pix4D, 2017b). After the desired parameters are defined, the project may be processed with the desktop version or uploaded to the cloud (Pix4D, 2017b). If the cloud is used, the results may be downloaded for further processing and re-processing until desired results are achieved. Manual tie point, MTP, may be added in order to improve the automatically processed point cloud. The processed model may also be forced to have a certain orientation, absolute orientation (Pix4D, 2017b). From the generated models it is possible to make e.g. orthophotos and index maps (Pix4D, 2017b).

3.3.1 Outline of processing steps

Pix4D mapper consists of three main processing steps:

1. Initial processing
2. Point Cloud and Mesh
3. DSM, Orthomosaic and Index

Step 1 is necessary to create index maps, while both step 1 and 2 are needed to create the orthophotos. In step 1, the software identifies the specific features in the images as keypoints (Pix4D). These keypoints are then matched with a similar keypoint in other images (Pix4D). The necessary overlap percentage between the images may differentiate depending on the image scene (Pix4D). For projects consisting of thermal images, an overlap of 90 % may be required (Pix4D). The internal and external parameters of the camera are also calibrated in this step (Pix4D). The product of this step is a three-dimensional ray-cloud consisting of automatic tie points (Pix4D).

Step 2 builds upon the automatic tie points found in step 1, creating a densified point cloud (Pix4D). The densified point cloud consists of additional tie points created on the basis of the automatic tie points (Pix4D). A three-dimensional texture mesh can be created from the densified point cloud (Pix4D). Figure 3.1 displays the results from step 1 and 2.
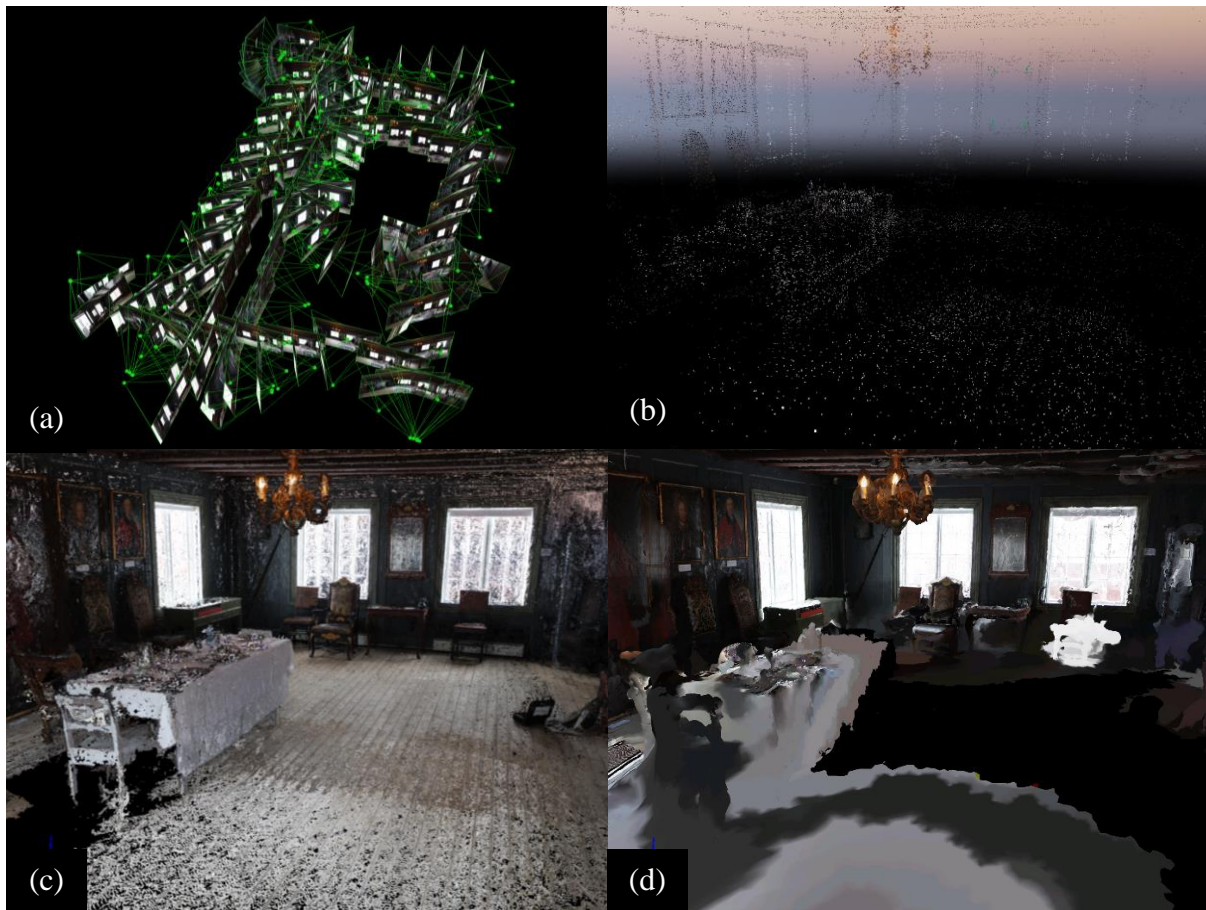
Figure 3.1: The results from step 1 and 2 are; (a), the resulting images orientations, (b), the automatic tie points, (c), the point cloud, and (d), the triangle meshes.

3.3.2 Mapping

How images are obtained can greatly affect the generated products from the photogrammetry. The exterior orientation of the camera may affect the number of matched points between images. This also applies to Pix4Dmapper.

A shooting angle perpendicular to the wall is considered the best method to achieve the most numerous and well-distributed matches in Pix4Dmapper (Pix4D, 2017a). Different angles, both vertically and horizontally, usually result in less matches among images (Pix4D, 2017a).

Another element to be considered is how the operator move compared to the photographed surface. The operator should always face perpendicular to the measured area, as this is considered the best option for most spaces (2017a). This result in less distortion in the images as the area of interest appears at the center (2017a).

Indoor mapping is often considered more challenging than outdoor mapping because of restricted space, dim light conditions and flat surfaces with few definite details (2017a). The method may also be applied to areas outside with similar challenges.

4.Methodology

This chapter presents the historical building, Snekkenes, at which the case study was performed, section 4.1, the data collection, section 4.2, and data processing, section 4.3.

4.1 Snekkenes

A case-study of Snekkenes was performed at Borgarsyssel Museum in Sarpsborg, Norway. Borgarsyssel Museum is an open-air museum founded in 1921 with a county-wide collection of building masses from Østfold, stretching from world war II and all the way back to the Middle Ages (*Borgarsyssel museum*). A remarkable collection of historical artifacts ranging from the Stone Age and up to our own time is also housed and displayed at the museum (*Borgarsyssel museum*).

The historical building, Snekkenes is an Empire style wooden building from the latter half of the 18th century, was the first building moved to Borgarsyssel Museum (Jensen). There are several portraits displayed at Snekkenes, as well as furniture in Baroque, Rococo and Empire style (Jensen).

In May 2016, an inspection of Snekkenes was performed (Borgarsyssel Museum, 2016). The furniture and ceiling in the Werenskiold-hall were inspected and mold was found on several furnitures. This also includes mold previously revealed on furniture during seasonal cleaning (Borgarsyssel Museum, 2016). Most of the furniture, paintings and objects on the first floor were inspected in June 2016 (Borgarsyssel Museum, 2016). It was then found that 59 objects were exposed to mold in varying degrees (Borgarsyssel Museum, 2016).

4.2 Data collection

The first part of this section describes how thermal and visual images were acquired at Snekkenes. The second part, section **Feil! Fant ikke referansekilden.**, deals with the data collection using the heat flow meter method. Section 4.2.3 describes the indoor and outdoor atmospheric measurements taken at Snekkenes.

The data were collected during the winter in the time frame from February 6 to February 9. In good time before the data were to be collected, the electric radiators at Snekkenes were set to 20 °C. This was in order to acquire a sufficient temperature difference between the indoor and outdoor needed for the following data acquisitions.

4.2.1 Image acquisition

There were acquired two sets of images from the photographic surveys performed at Snekkenes. The first set of images acquired were visual images of Snekkenes with the use of CANON EOS 100D. The second set of images were thermal images acquired using FLIR T620bx. Both cameras were equipped with perspective lenses.

<center>(a)   (b)   (c)</center>
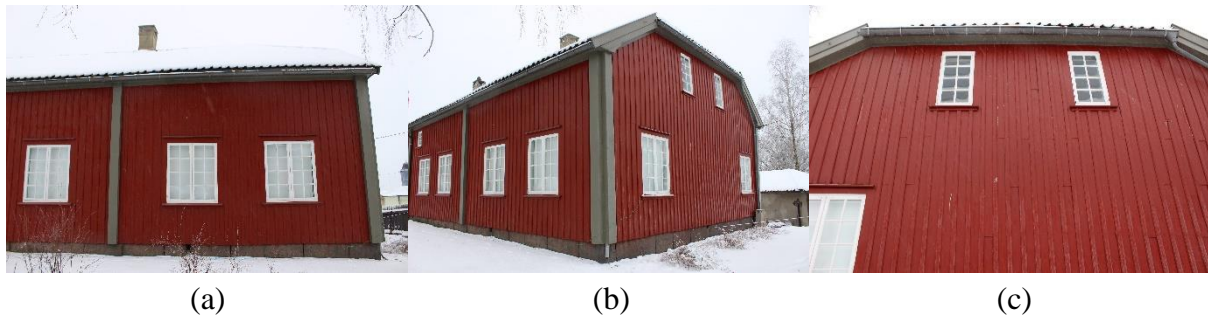
Figure 4.1: Image taken (a) perpendicular to the wall, and (b) with a horizontal and (c) with a vertical angle different from 90 degrees to the wall.

The indoor survey of Snekkenes was done in Werenskiold-hall, while the outdoor survey included the facades corresponding to Kontoret and Werenskiold-hall. All the images were acquired using the same method with an operator manually photographing both the indoor and outdoor surfaces of the selected areas. The operator moved systematically and in parallel with the wall, maintaining a perpendicular shooting angle towards the photographed surface at most times. In corners and areas beyond the operator's reach, the shooting angle differed from 90 degrees to the wall, see figure 4.1. In some areas, it was especially difficult to acquire good images as the distance between the operator and the photographed surfaces were restricted by obstacles. These obstacles could, for example, by other buildings and vegetation outdoor, see figure 4.2, and furniture and walls indoor.
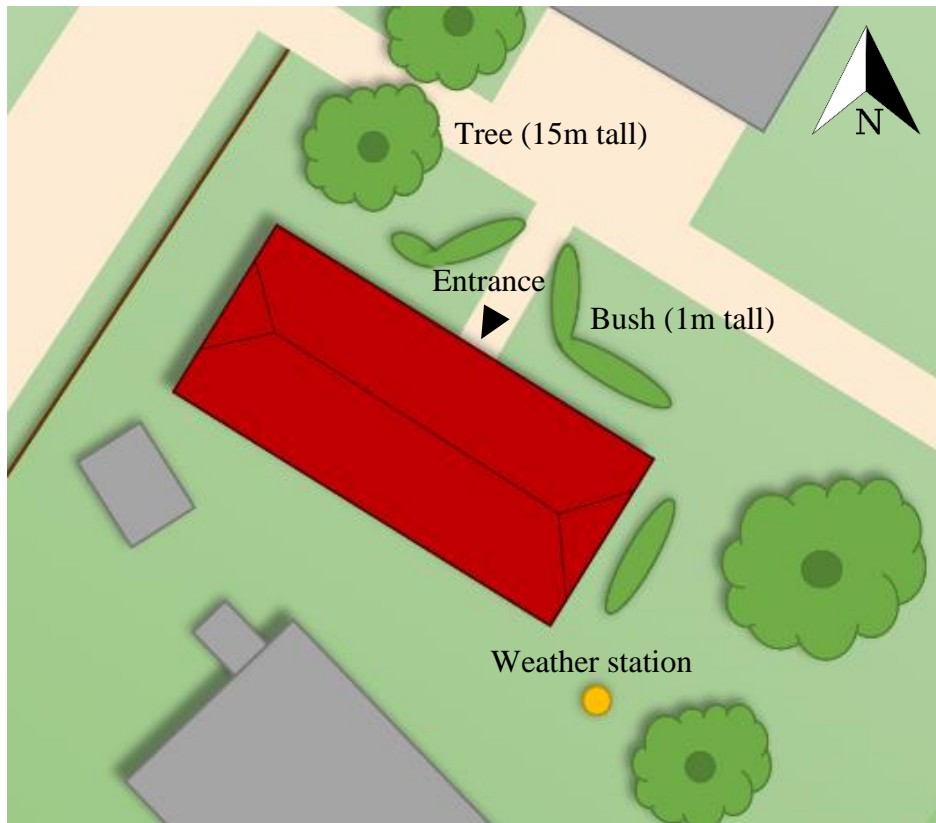
Figure 4.2: Illustrative image of different obstacles located around Snekkenes.

4.2.1.1 The thermographic survey

During the outdoor thermographic survey, the weather was cloudy with a wind speed of 0.73 m/s. The atmospheric temperature indoor was 13.5 °C, while the atmospheric temperature outdoor was -0.6 °C. For the indoor survey of Werenskiold-hall, the atmospheric temperature was 13.5 °C indoor and -1.5 °C outdoor, as well as an atmospheric relative humidity of 34.5 % indoor and 91 % outdoor. These parameters were of importance for the further processed results based on the thermal images.

During the thermographic survey, the artificial light sources and some of the electric radiators were turned off, while the blinds were always kept down. Two portraits were selected in order to acquire thermal images of surfaces that were covered by historical items. The thermal images were taken immediately after the portraits were removed. Figure 4.3 displays the selected portraits, where the larger portrait is of Major Jens Werenskiold (Jensen). This portrait is of such scale, that it touches the floor and nearly reaches the ceiling.

The thermographic survey was a time-consuming process as the infrared camera had a long response time. Another time-consuming aspect of this survey was the vertical sectioning of the walls. Indoor, the walls had to be sectioned at least four times vertically, in order to capture the whole height of the wall. A total number of 940 thermal images were acquired during the survey, where 524 were taken indoor and 416 were taken outdoor.

Figure 4.3: The two portraits that were removed during the thermographic survey.

Before the thermographic survey was executed, certain camera settings were managed based on the atmospheric measurements taken a little while before the survey. For the indoor survey, a temperature interval from 5.0 to 20 °C was set. The surface emissivity was estimated to be 0.95, based on table 2.1, for all surfaces inside and outside. Other parameters supplied to the camera differed between the indoor and outdoor thermographic survey. For the atmospheric conditions, the temperature was set to 15 °C and the relative humidity to 30 %. The average working distance between the camera and the surface was set to 5 meters for the indoor survey. Other camera parameters, as well as the outdoor camera parameters, are displayed in table 4.1.

Table 4.1: Camera settings during surveys.

	Temperature interval	Emissivity	Atmospheric temperature	Atmospheric relative humidity	Reflected temperature	Average working distance
Indoor	5.0 –19.9 °C	0.95	15.0 °C	30 %	15.0 °C	5.0 m
Out-door	- 5.0–10.0 °C	0.95	- 5.0 °C	40 %	0.0 °C	10.0 m

4.2.1.2   The visual survey

For the visual images, CANON EOS 100D was used. The camera was set to manual exposure for the indoor survey. The cameras shutter speed, or exposure time was set to 1/40 seconds and the aperture was set to F3.5. For the outdoor survey, the camera was set to automatically select the shutter speed and aperture in order to acquire the best images. The flash setting was turned off for both the indoor and outdoor visual survey.

In order to acquire good lighting conditions during the visual survey indoor, the blinds were rolled up. The visual survey was less time-consuming as the camera used had a more immediate response time. A total number of 2346 visual images were acquired during the survey, where 904 were taken indoors and 1442 were taken outdoors.

4.2.2   The heat flow meter method

● TRSYS01 sensors

● EasyLog USB Data Logger
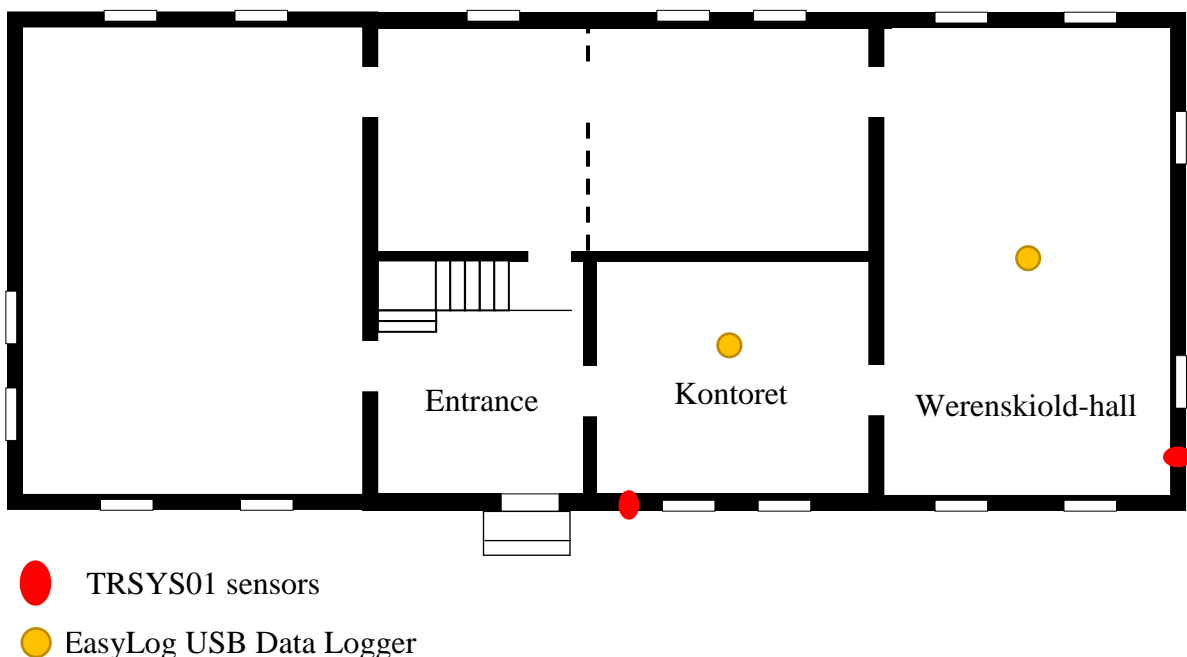
Figure 4.4: The location of the TRSYS01 sensors and the atmospheric measuring equipment. Modified figure from (Jensen).

The TRSYS01 was used for the in-situ measurements with the heat flow meter method. The sensors were mounted to one wall in Werenskiold-hall and another wall in Kontoret, see figure 4.5. A double-sided "removable" carpet laying tape was recommended in TRSYS01 user manual for mounting the sensors on walls. Because of the historical value of the building, this recommended fastening method was not approved by Borgarsyssel museum. Another fastening method, using existing nails on the wall surface, had to be applied indoor. Outdoor, the sensors were fastened with the use of drawing pins.
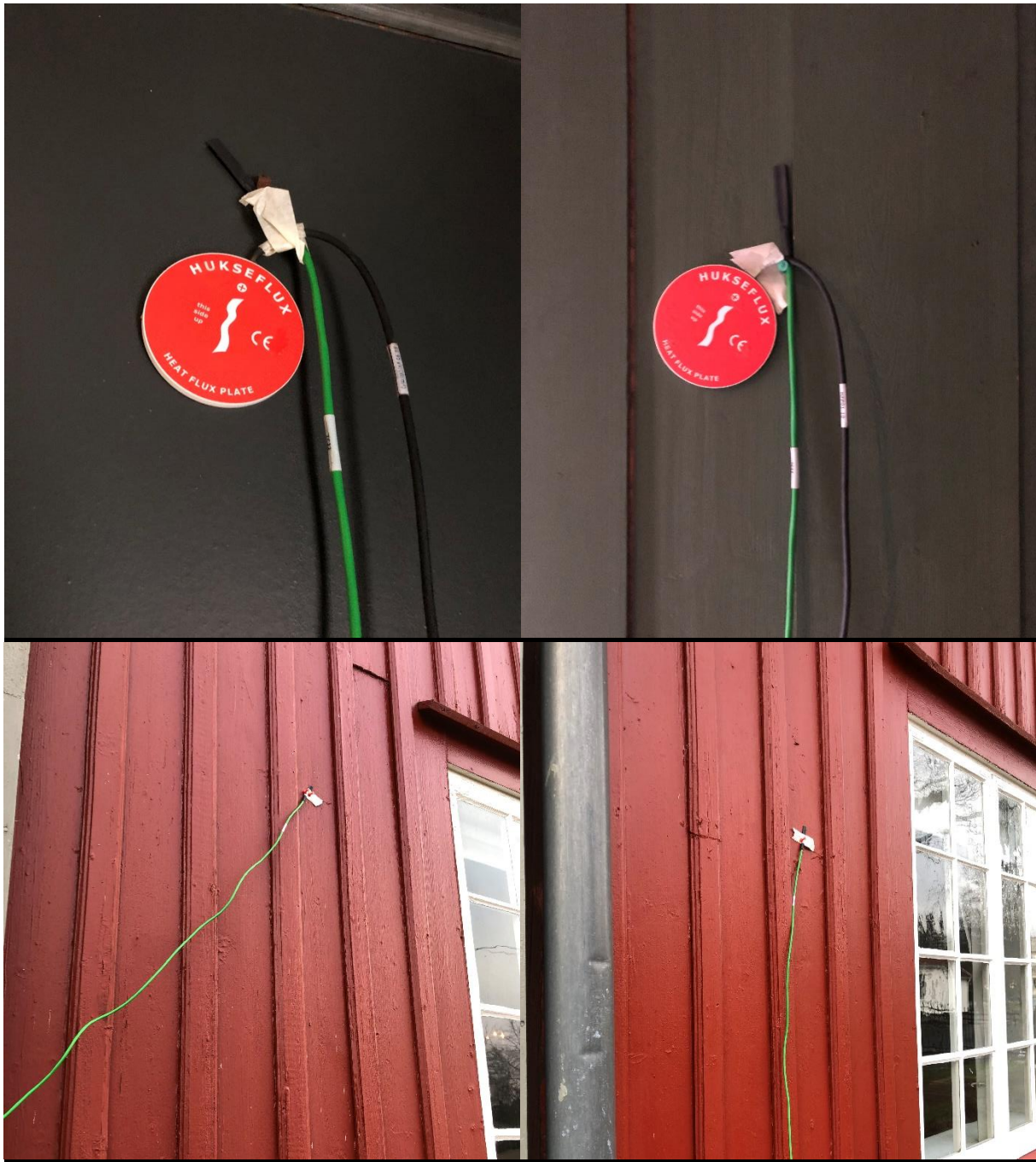
Figure 4.5: The sensors mounted the walls in Werenskiold-hall (the left side), and Kontoret (the right side).

Thermal images were taken of the wall section prior to mounting of the sensors, which was in order to avoid thermal bridges or irregularities in the wall. The indoor set of sensors, consisting of a HFP01 sensor and one TC, were then placed on a homogeneous wall section. The sensors were placed a reasonable distance away from any thermal bridges, cooling and heating devices, and cracks. One of the two electric radiators in Kontoret had to be turned off as it was too close to the sensors. The window blinds were down, and artificial light sources were turned off in both rooms during the measuring period. The sensors mounted outdoor were placed at the same location as the indoor sensors. Measurements of the heat flux, and indoor and outdoor surface temperature were logged for every 10 minutes during the measured period.

4.2.3 The atmospheric measurement

In order to measure the atmospheric conditions at Snekkenes, atmospheric measuring equipment was installed indoor and outdoor. Indoor the EasyLog USB Data Logger was installed, see figure 4.4, which logs the atmospheric temperature and relative humidity.

A weather station was installed outdoor, see figure 4.2. VP-4, a low-maintenance sensor, was installed in order to measure atmospheric temperature, relative humidity, barometric pressure, and vapor pressure (Environment). This sensor does not require writing or programming and can be mounted directly to a data logger mast (Environment). The VP-4, in this thesis, was connected to EM60 Solar-Powered Data Logger. ATMOS 22 Ultrasonic Anemometer was also installed on the weather station in order to measure the wind speed.

The installation of the equipment and retrieval of the measured data were done by master student Ines Haga (Haga, 2019), though the further processing was done by the author.

4.3 Data processing

The further process of the acquired data from section 4.2 can be divided into three main parts, which is the processing of the thermal images, section 4.3.1, the visual images, section 4.3.2, and the heat flow meter method, section **Feil! Fant ikke referansekilden.**.

4.3.1 The processing of the thermal images

As the emissivity of the wall surface was implanted into FLIR T620bx, the infrared camera corrected the walls kinetic temperature when the images were taken. Other surfaces, with different emissivities, were not corrected as the walls were the main aim of this thesis. The thermal images were used in order to calculate the wall's relative humidity on the surface and thermal transmittance.

In order to retrieve the correct relative humidity on the surface, the atmospheric measurements measured during thermographic surveys were used. From the atmospheric measurement, the dew point temperature was determined, equation (2.5). This was then used in order to find the relative humidity on the surface, equation (2.6).

The thermal transmittance was also found with the use of the atmospheric measurements measured during the surveys. Equation (2.25) was used in order to calculate the thermal transmittance from the temperature readings of the walls. As the emissivity was close to 1, the reflected temperature, T_{Ref}, was set equal to the atmospheric temperature. The internal convective heat transfer coefficients, equation (2.29), was used for the indoor images. For the thermal images taken outdoor, the convective heat transfer coefficients, equation (2.28), was used.

In order to generate images and maps of the relative humidity and thermal transmittance, MATLAB and Pix4Dmapper were used. Calculate and then generate images and maps of the thermal readings.

4.3.1.1 *Singular images*

For the generating of singular images, the thermal images were converted into csv-files with the use of FLIR Tools, a software for importing, editing and analyzing images (FLIR). This converted the thermal images into plain-text files, which could be further processed in MATLAB, a programming platform. MATLAB version R2019a was used in this thesis.

Two scripts were made in order to calculate and convert the csv-files into images. For the thermal images indoor, the csv-files were calculated and converted into images of the wall's relative humidity on the surfaces and thermal transmittance. Outdoor, the thermal images were only calculated and converted into images of the wall's thermal transmittance. A new set of thermal images were also generated in order to have the same color scale as the temperature maps generated in Pix4D. The scripts can be found in appendix 9.3.

4.3.1.2 *Maps*

The processing of generating maps, from the thermal images, were done with Pix4Dmapper, version 4.3.31. In comparison to the singular images, the thermal images were not converted into plain text before they were implanted into Pix4Dmapper. This is because Pix4Dmapper is capable of creating reflectance maps from thermal images. Each pixel in a reflectance map faithfully indicated the reflected values of each pixel of the object (Pix4D, 2017b). The projects could only contain images of one wall and had to have an absolute orientation in the xy-plane in order to further process the reflectance maps. If the generated project had a different absolute orientation, the wall would not be shown in the index map calculator in Pix4D.

From the reflectance maps, index maps were generated, which are false-color image where each pixel is a calculated value based on the reflectance map (Pix4D, 2017b). For the indoor walls, maps were made of the wall surface temperature, the relative humidity on the surface and the thermal transmittance. Outdoor, only the temperature and thermal transmittance maps were generated. The linear thermal bridge was also calculated for one thermal bridge on wall O2 with the use of the thermal transmittance calculated at the same location as the sensors were mounted in Werenskiold-hall. The wall's location can be found in figure 5.1.

4.3.2 Processing of the visual images

The visual images were processed in Pix4D in separate projects from the thermal images. This was because attempted merging of the project did not give acceptable results.

28

The three-dimensional model, made from the visual images, were used in order to generate Orthophotos. Orthophotos, of selected internal walls and external facades, were generated after processing steps 1 and 2. To generate an orthophoto of the facades, surfaces were defined to indicate the facades' three-dimensional orientation in the point cloud. The orthoplanes were then inserted into the point cloud and aligned with the corresponding surfaces. Figure 4.6 illustrates the aligned orthoplane with the defined surface of the facade. The orthoplanes were adjusted appropriately to the corresponding facade if they did not align properly. Orthophotos were then generated with a recommended resolution set by Pix4D.

Figure 4.6: The aligned orthoplane with the defined surface for an interior wall.

4.3.3 The heat flow meter method

The measurements acquired, with the heat flow meter, during the day were not used in order to determine the following calculations.

The thermal resistance of the two walls elements were calculated using equation (2.30). In order to determine the total thermal resistance at the two locations, the interior and exterior surface thermal resistance were also calculated. For the interior surface thermal resistance, equation (2.33) was used whit h_c equal equation (2.29). The average temperature difference was calculated from the measurements taken over the three subsequent nights. As for the exterior surface thermal resistance, equation (2.33) was used whit h_c equal equation (2.28). Only the wind speeds measured at nighttime were used in order to find the average wind speed for the three subsequent nights. With this, the total thermal resistance was calculated and used in order to determine the thermal transmittance of the wall.

5. Results

This chapter presents the results in six main parts. The first section presents the results achieved from Pix4RD. Section 5.2 deals with the results found from the surfaces found underneath the removed portraits. The atmospheric measurements, from the measured period, is presented in section 5.3, while section 5.4 deals with the measurements from the heat flow meter. In section 5.5, the thermal transmittance based on the heat flow meter method, while section 5.6 deals with the comparison of the thermal transmittance achieved from the thermography and the heat flow meter method.

5.1 Large wall sections

This section presents the five wall sections produced from Pix4D. The locations of the walls can be found in figure 5.1.
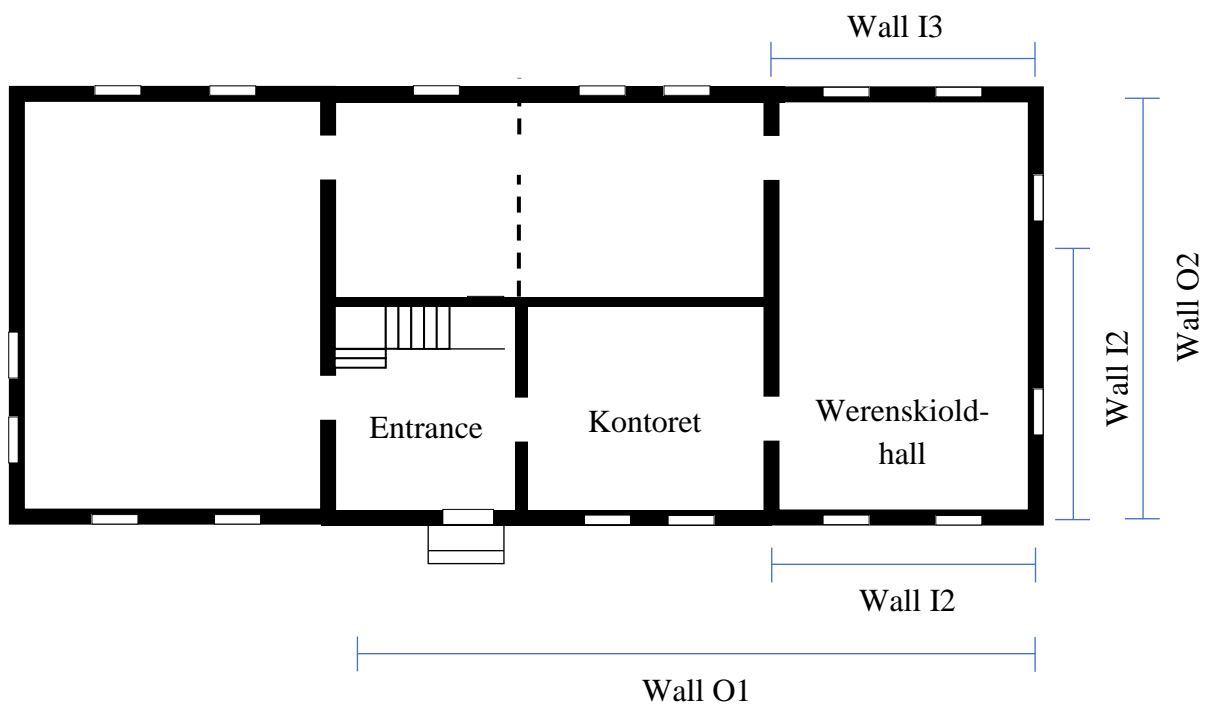

Figure 5.1: The locations of the walls processed in Pix4D. Modified figure from (Jensen).

5.1.1 Wall I1

The thermal map, figure 5.3 (a), displays a fluctuation in temperatures across the surface of wall I1. Areas closer to the ceiling have temperatures around 11 – 13 °C, while the areas closer to the floor have temperatures between 5 – 9 °C. The highest temperatures are found in the areas close to the electric radiator, which is turned on, located on the right side of figure 5.2. In these areas, the temperatures are around 18 – 19 °C. Areas above this electric radiator also have higher temperatures than other areas at the same height, with a temperature range of 14 – 17 °C.

The mirror located between the two windows, see figure 5.2, has slightly higher temperatures than the wall surface in the same area, figure 5.3 (a). Additionally, the surface temperature in the area below the mirror is slightly lower than other areas in the same height. Other wall decorations and furniture also have slightly warmer surfaces than the wall surface in the same area.

Figure 5.3 (b) displays higher values of thermal transmittance closer to the floor, ranging from 1.2 to 1.5 W/m^2K. Areas closer to the ceiling have lower values between 0.1 to 0.3 W/m^2K. Objects, such as chairs and wall decorations, also have lower values of thermal transmittance than the wall surfaces at the same location. Overall, there are strong fluctuations in the calculated thermal transmittance of wall I1.

Figure 5.3 (c) displays that most of the surfaces in the areas close to the floor have a relative humidity close to 45 %. In some of these areas, beneath the furniture, the relative humidity is up to 60 %. At the ceiling, the relative humidity on the surface is around 35 % to 40 %. There is also a slight increase in the relative humidity on the surface below the mirror, compared to the surfaces in the same area. Areas located above and close to the electric radiator to the left have the lowest values of relative humidity on the surfaces, with values around 30 %.

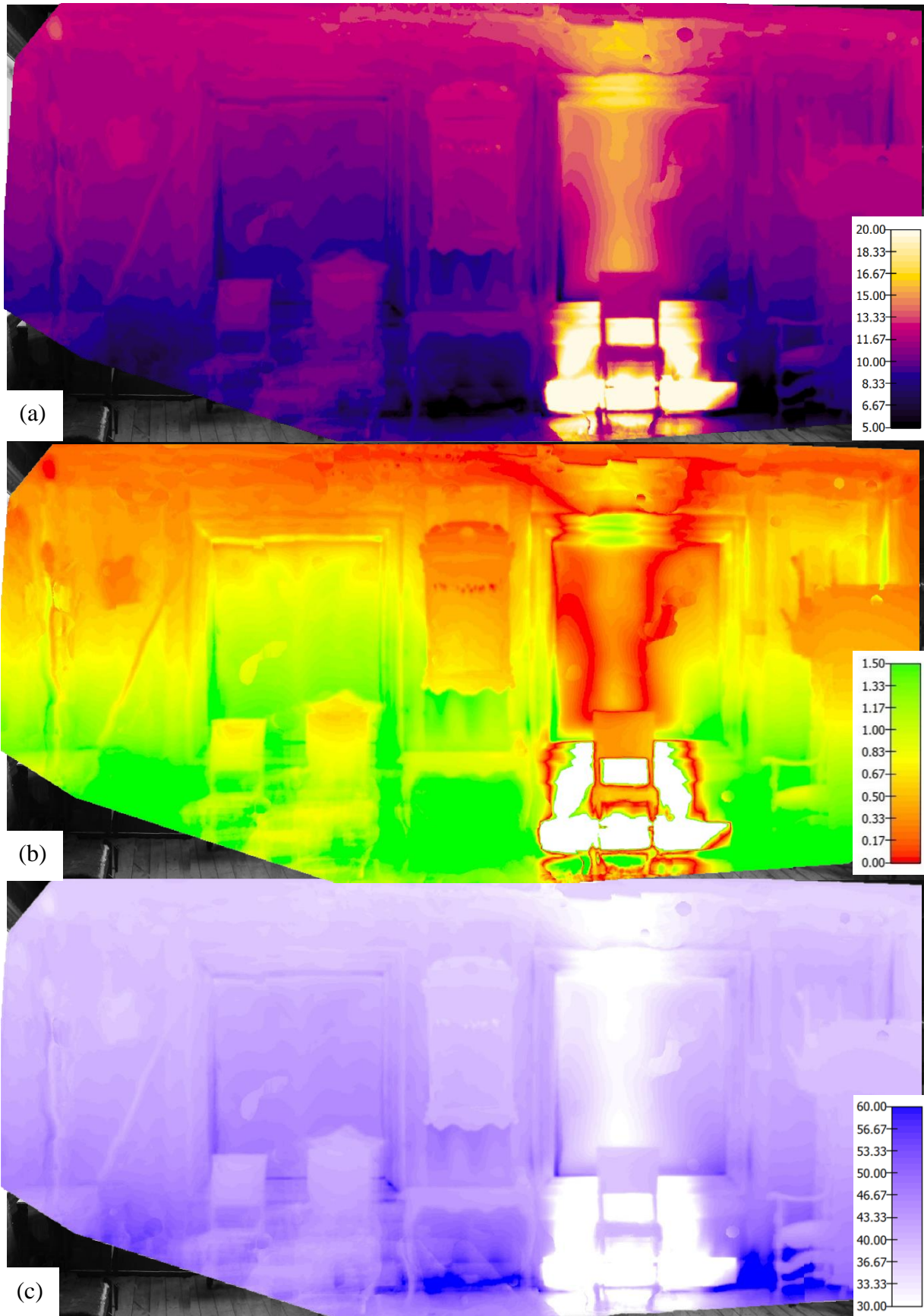Figure 5.2: The visual orthophoto of wall I1.

Figure 5.3: (a) is the thermal map, (b) is thermal transmittance map and (c) is the map of the relative humidity on the surface of wall I1.

5.1.2 Wall I2

In the thermal map of wall 12, figure 5.5 (a), the areas closer to the ceiling have temperatures between 12 – 14 °C, while the lower areas closer to the floor have a temperature around 5 – 10 °C. It is a steady decrease in the wall's surface temperature from the ceiling to the floor. Furniture and paintings have a slightly higher temperature than the wall surfaces in the same area.

In figure 5.5 (b), the thermal transmittance in the areas at the ceiling are a little lower than what was displayed in figure 5.3 (b), ranging from 0.2 to 0.4 W/m²K. It is a steady increase in the thermal transmittance, on the wall surface, from the ceiling and down to the floor. By the floor, the thermal transmittance is at its highest with values around 1.2 to 1.5 W/m²K. Furniture and wall decorations a have lower thermal transmittance compared to the areas at the same height.

As in figure 5.3 (c), figure 5.5 (c) displays a relative humidity on the wall surface of up to 60 % at the floor. Higher up on the wall, the relative humidity decreases to around 40 %. The relative humidity on the surface of the wall decorations and furniture are slightly lower than other areas in the same height.

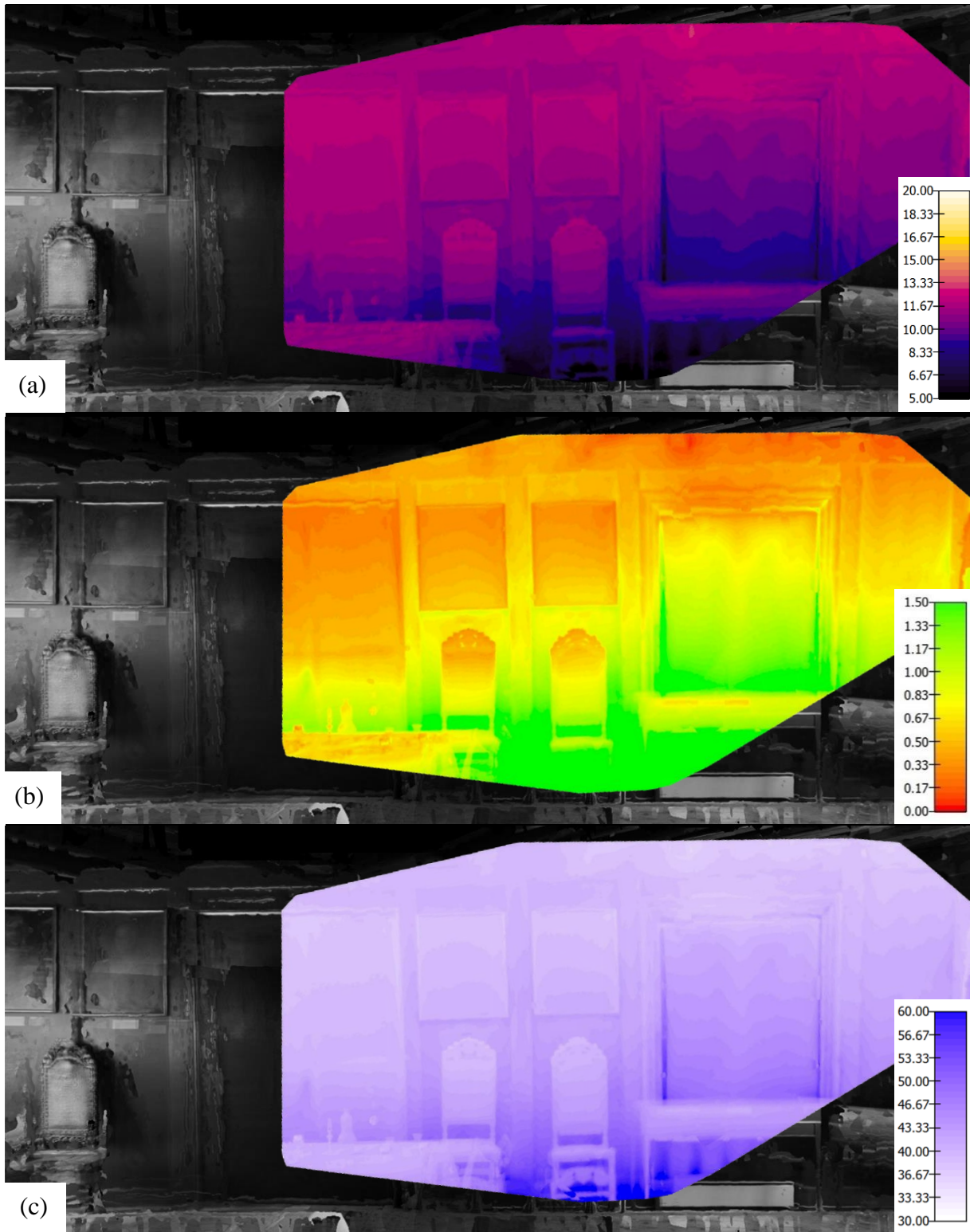*Figure 5.4: The visual orthophoto of wall 12.*

Figure 5.5: (a) is the thermal map, (b) is the thermal transmittance map and (c) is the map of the relative humidity on the surface of wall I2.

5.1.3 Wall I3

Figure 5.7 (a) displays a fluctuation in the surface temperature across wall I3. The surface temperatures, by the floor, are around 7 – 11 °C, while areas closer to the ceiling have temperatures of 12 – 14 °C. In the areas close to the electric radiator, which is turned on and located to the left in figure 5.6, the temperatures are around 18 – 19 °C. The areas above this electric radiator have temperatures of 15 – 17 °C.

Figure 5.7 (b) displays lower values of thermal transmittance at the wall surfaces beneath the ceiling, ranging from 0.1 to 0.3 W/m^{2}K. As the distance from the ceiling increases, the thermal transmittance also increases. By the floor, the thermal transmittance is around 1.2 to 1.5 W/m^{2}K. Furniture and wall decorations have a lower thermal transmittance than the surfaces at the same height. The areas closer to and above the radiator to the left have the lowest values of thermal transmittance compared to other surfaces at the same height.

Overall, the relative humidity on the surface of wall I3, see figure 5.7 (c), has low values from around 35 – 40 %. By the floor, the relative humidity on the surface is at its highest with values ranging from 50 – 60 %. The areas closer to and above the electric radiator to the left, which is turned on, have the lowest values of relative humidity in comparison to other surfaces at the same height. For the furniture and wall decorations, the relative humidity is slightly higher than the areas around.

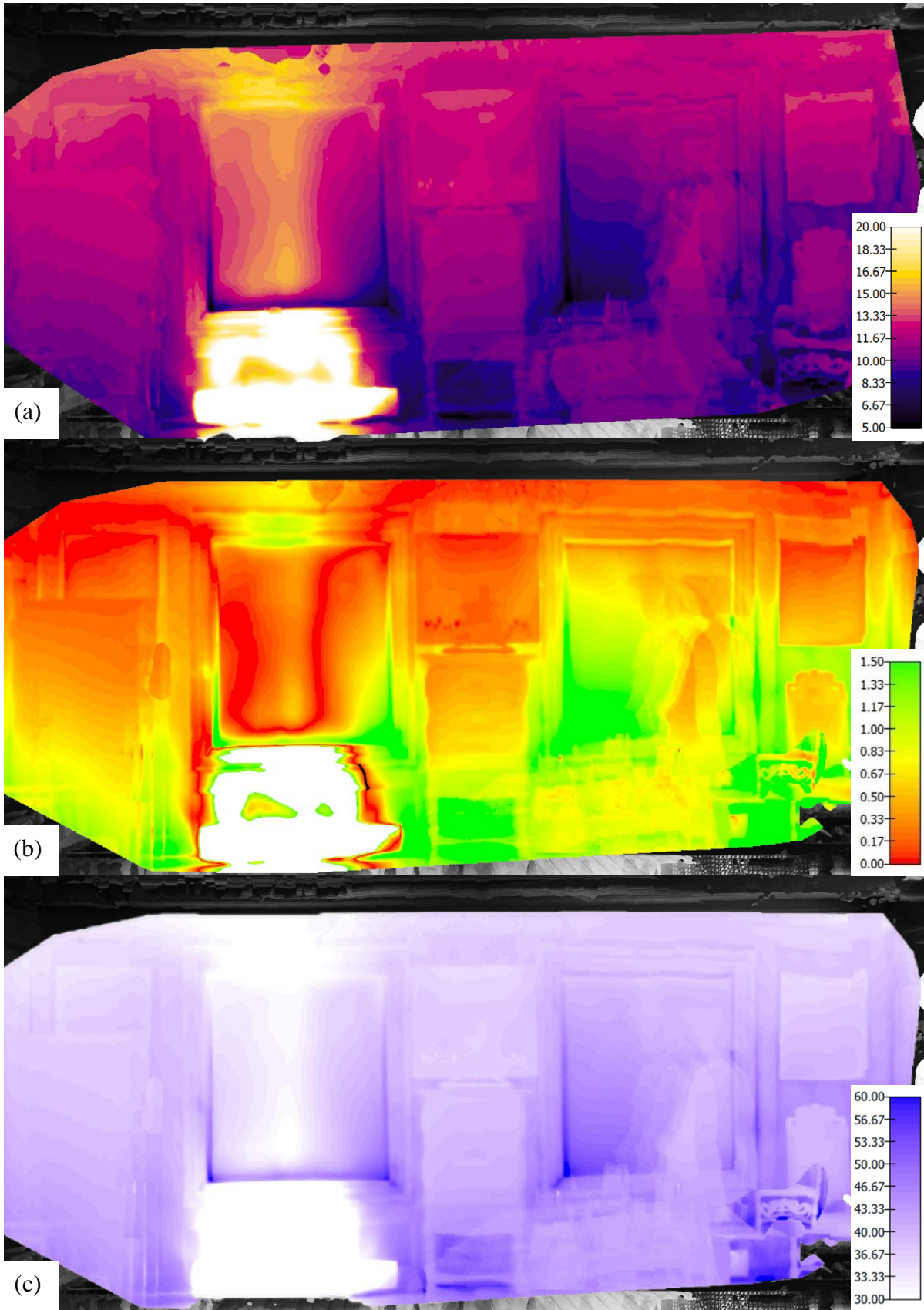*Figure 5.6: The visual orthophoto of wall I3.*

Figure 5.7: (a) is the thermal map, (b) is the thermal transmittance map and (c) is the map of the relative humidity on the surface of wall I3.

5.1.4 Wall O1

The thermal map in figure 5.9 (a) shows that the surface temperatures of the wall are around 0.0 to -1.0 °C. It is a difference between the surface temperature on the wall sections corresponding to the different rooms indoor. The wall section corresponding to Werenskiold-hall has the highest surface temperature, ranging from -0.5 to -1.0 °C, while the wall corresponding to Kontoret has a slightly lower surface temperature between -0.8 to -1.2 °C.

Figure 5.9 (b) displays a variation in thermal transmittance on Wall O1. Overall, the thermal transmittance is lower on the wall section corresponding to Werenskiold-hall in comparison to Kontoret. The average thermal transmittance, of the marked areas at Kontoret, was found to be 0.30 ± 0.05 W/m^{2}K. For the marked areas at Werenskiold-hall, the average thermal transmittance was equal 0.18 ± 0.08 W/m^{2}K.

| Entrance | Kontoret | Werenskiold-hall |

Figure 5.8: The visual orthophoto of wall O1.
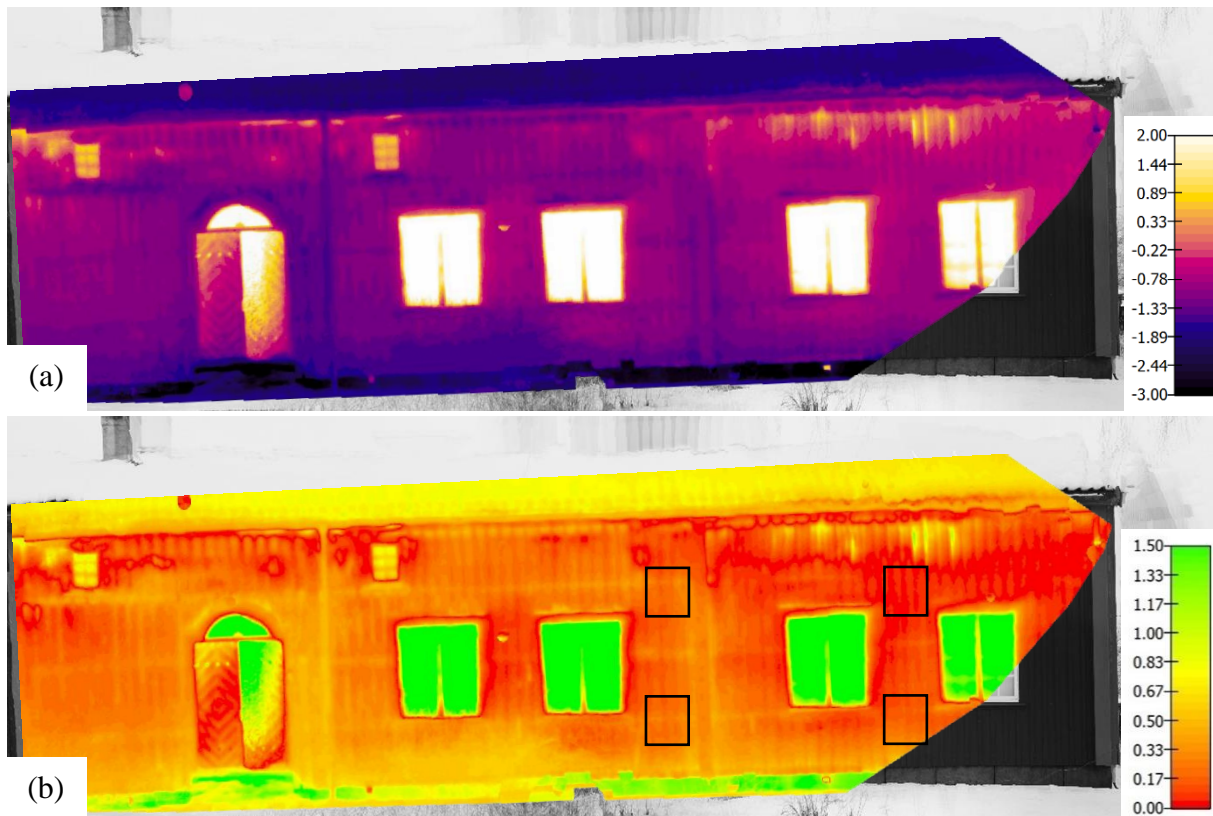
Figure 5.9: (a) is the thermal map and (b) is thermal transmittance map of wall O1.

5.1.4.1   The effect from vegetation

The difference in thermal transmittance and surface temperature in figure 5.9 might be caused by the vegetation around Snekkenes. In figure 4.2, there is a tall tree located not far from Werenskiold-hall. Because of the tree's location, a portion of the radiation emitted from Werenskiold-hall may be reemitted back to the wall surface, see figure 5.10, increasing the surface temperature and decreasing the thermal transmittance.
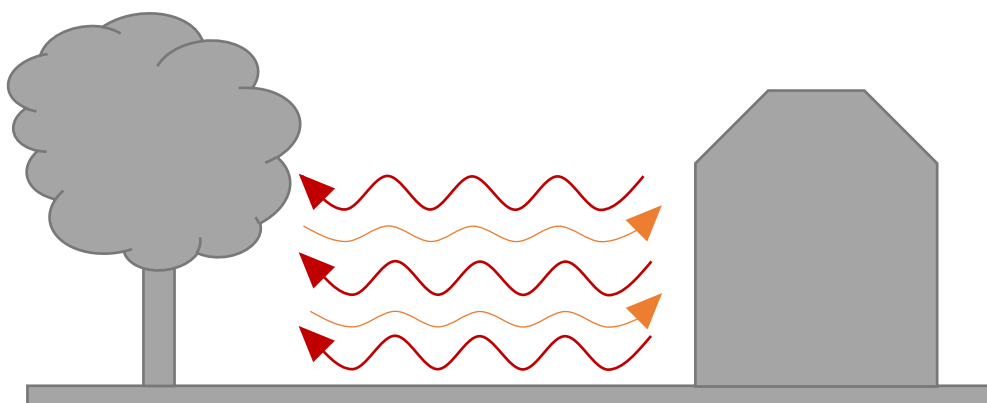
Figure 5.10: Illustration of the radiation emitted from Werenskiold-hall to the tree and the portion reemitted back to Werenskiold-hall.

5.1.5 Wall O2

Figure 5.12 (a) displays strong variations in the temperatures across the sectioned wall surface. This is especially the case for the areas located between the windows, on the upper floor, and the areas between the upper and lower floor. In these areas, the temperature ranges from 0.5 to 1.8 °C. The other areas on the wall have lower temperatures, with an average temperature of around -0.5 to 0.0 °C.

The thermal transmittance in figure 5.12 (b) shows there is a great variation in thermal transmittance across the sectioned wall surface. The area marked to the left in figure 5.15 (b) has an average thermal transmittance of 0.89 ± 0.26 W/m^{2}K. For the areas marked to the right in figure 5.15 (b), the average thermal transmittance is 0.23 ± 0.15 W/m^{2}K.

From figure 5.12 (b), the linear thermal transfer coefficient for the floor junction between the upper and lower floor, the marked area to the left, was estimated to be 0.0.94 W/mK. The calculations can be found in appendix 9.1. As it was uncertain how influenced the temperature the areas the floor junction around
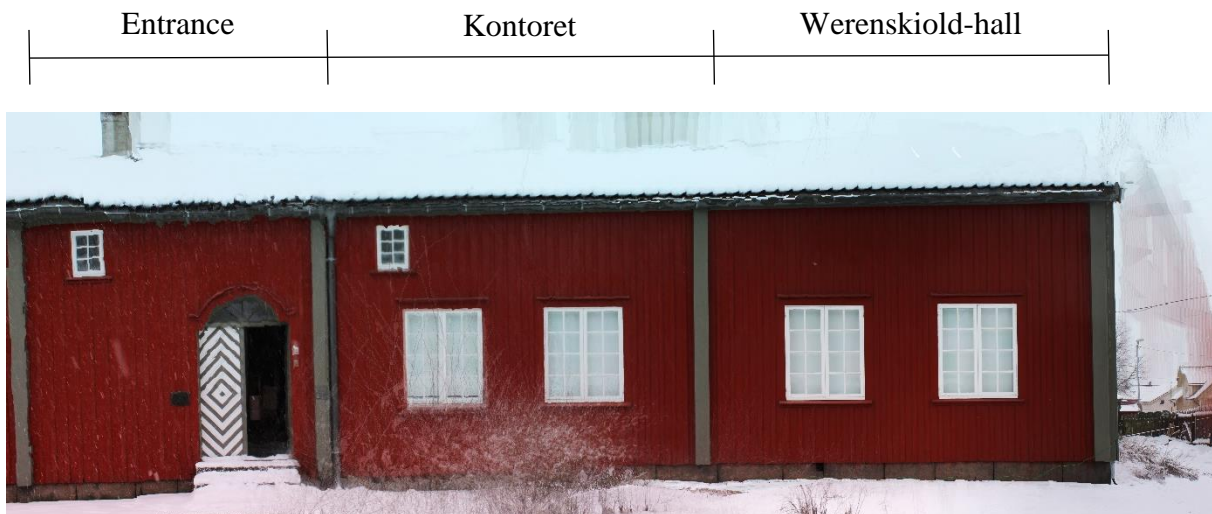

Figure 5.11: The visual orthophoto of wall O2.
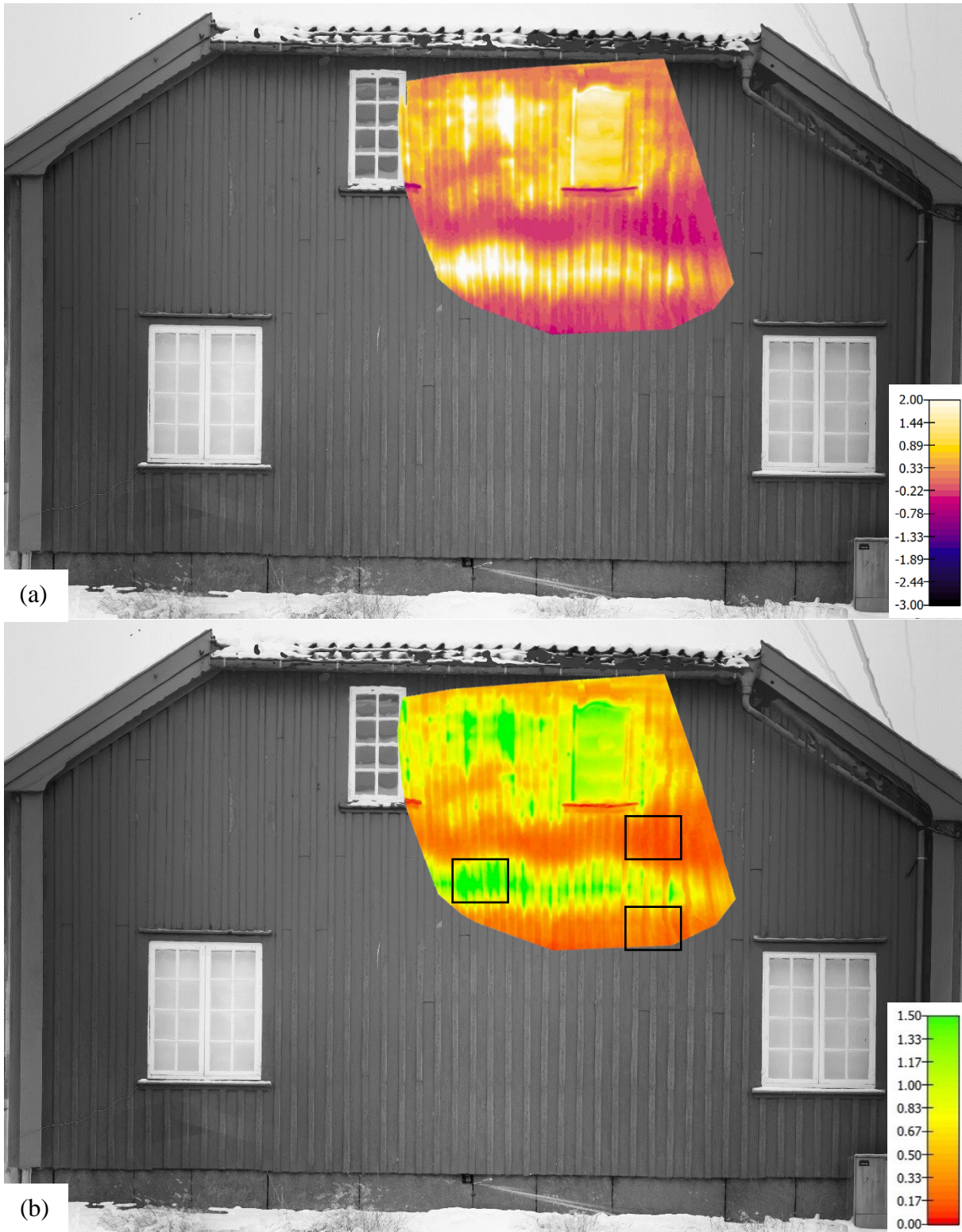
*Figure 5.12: (a) is the thermal map and (b) is thermal transmittance map of wall O2.*

5.2 The surfaces behind the portraits

5.2.1 Small portrait
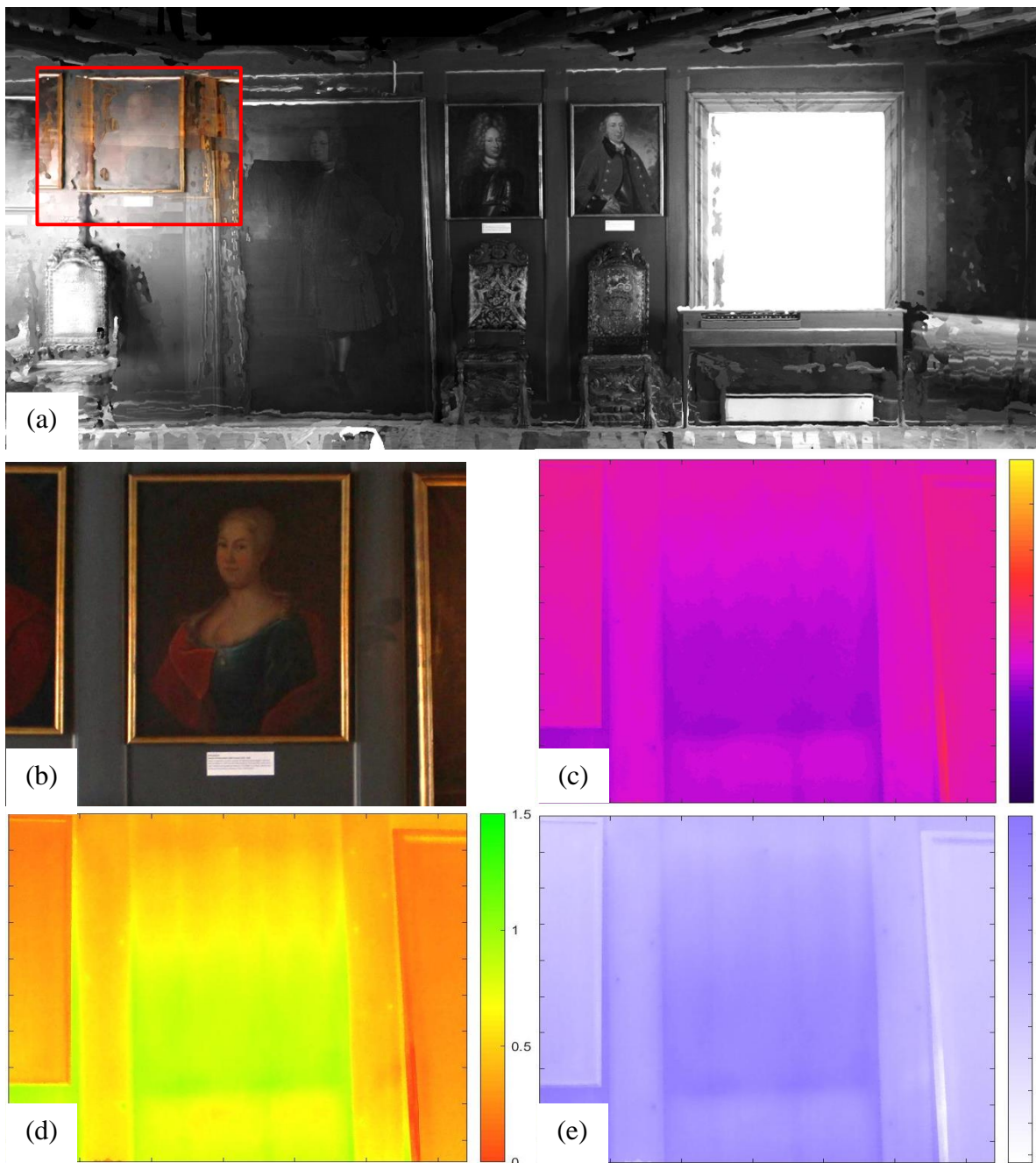
Figure 5.13: (a) is the location and (b) is an image of the small portrait, while (c) is the surface temperature, (d) is the thermal transmittance and (e) is the relative humidity on the surface behind the removed portrait.

Overall the surfaces behind the removed painting are different from the areas around it. This is especially the case at the lower regions where the portrait touched the wall surface. In this area, the difference is the largest between the surface behind the portrait and the other surfaces in the same height. The temperature in this area is 11-12 °C, while the thermal transmittance is around

0.9 W/m²K. As for the relative humidity, it is a few percent higher behind the portrait than the areas beneath it. The relative humidity is approximately 40 – 43 % behind the portrait.

5.2.2 Large portrait

Figure 5.14: (a) is the location and (b) is an orthophoto of a section of the large portrait, while (c) is the surface temperature, (d) is the thermal transmittance and (e) is the relative humidity on the surface of the corresponding area behind the portrait section.

Figure 5.14 (c) displays little to no temperature difference between the upper regions of the large portrait and the wall surface at the same height. The temperature is only slightly lower in this area, which has a range of 11 – 12 °C in the upper area and 9 – 10 °C in the lower area.

There are also only slight differences between the thermal transmittance and relative humidity on the surface behind the portrait, in comparison the other surfaces at the same height. The thermal transmittance, behind the portrait, in figure 5.14 (d) ranges from $0.3 - 0.6$ W/m^{2}K in the upper areas and from $1 - 1.5$ W/m^{2}K in the lower area. In the higher areas, the relative humidity, displayed in figure 5.14 (e), is between $38 - 42$ %. There is a steady decrease in relative humidity in the lower areas, where it ranges from $44 - 49$ %.
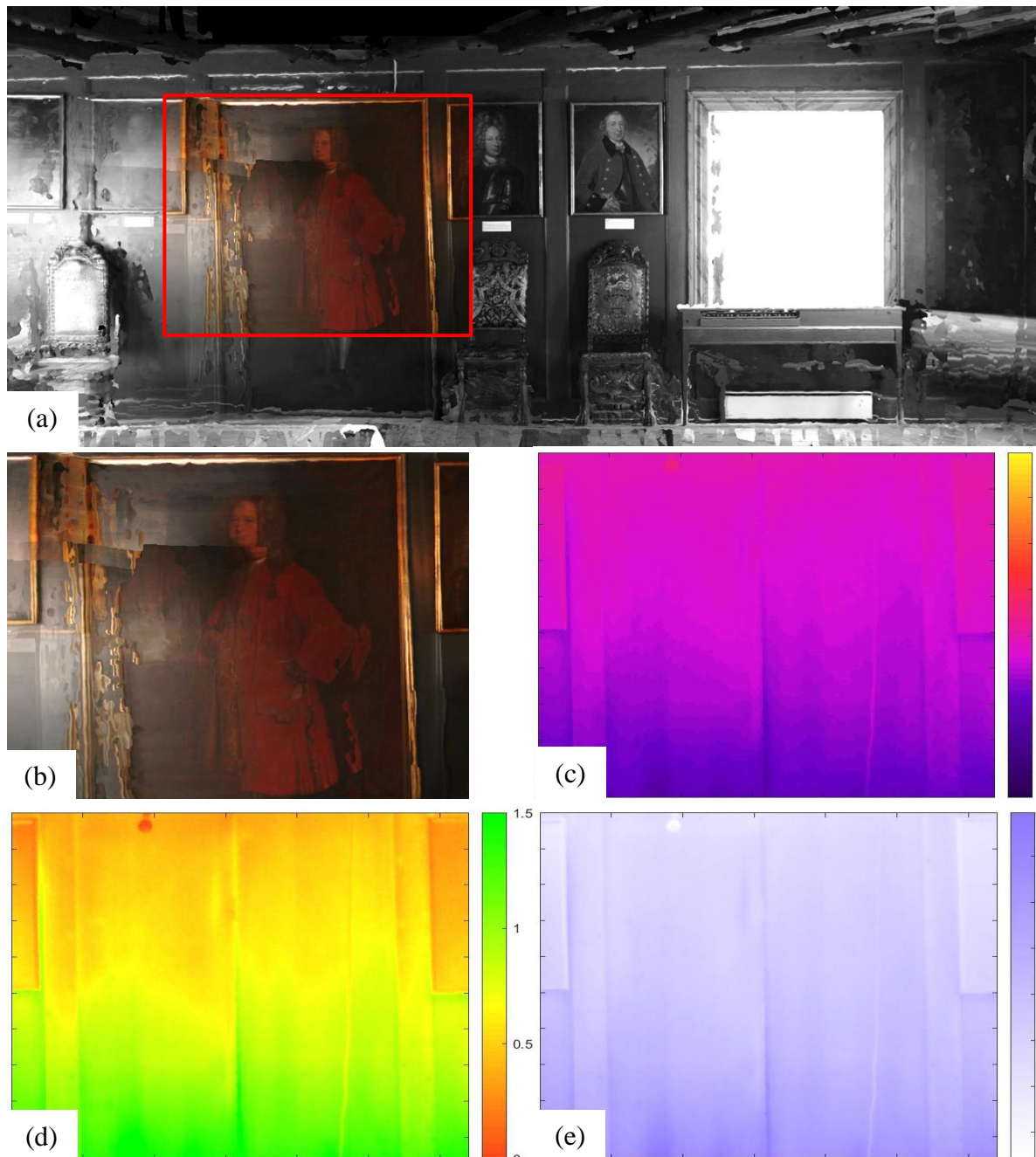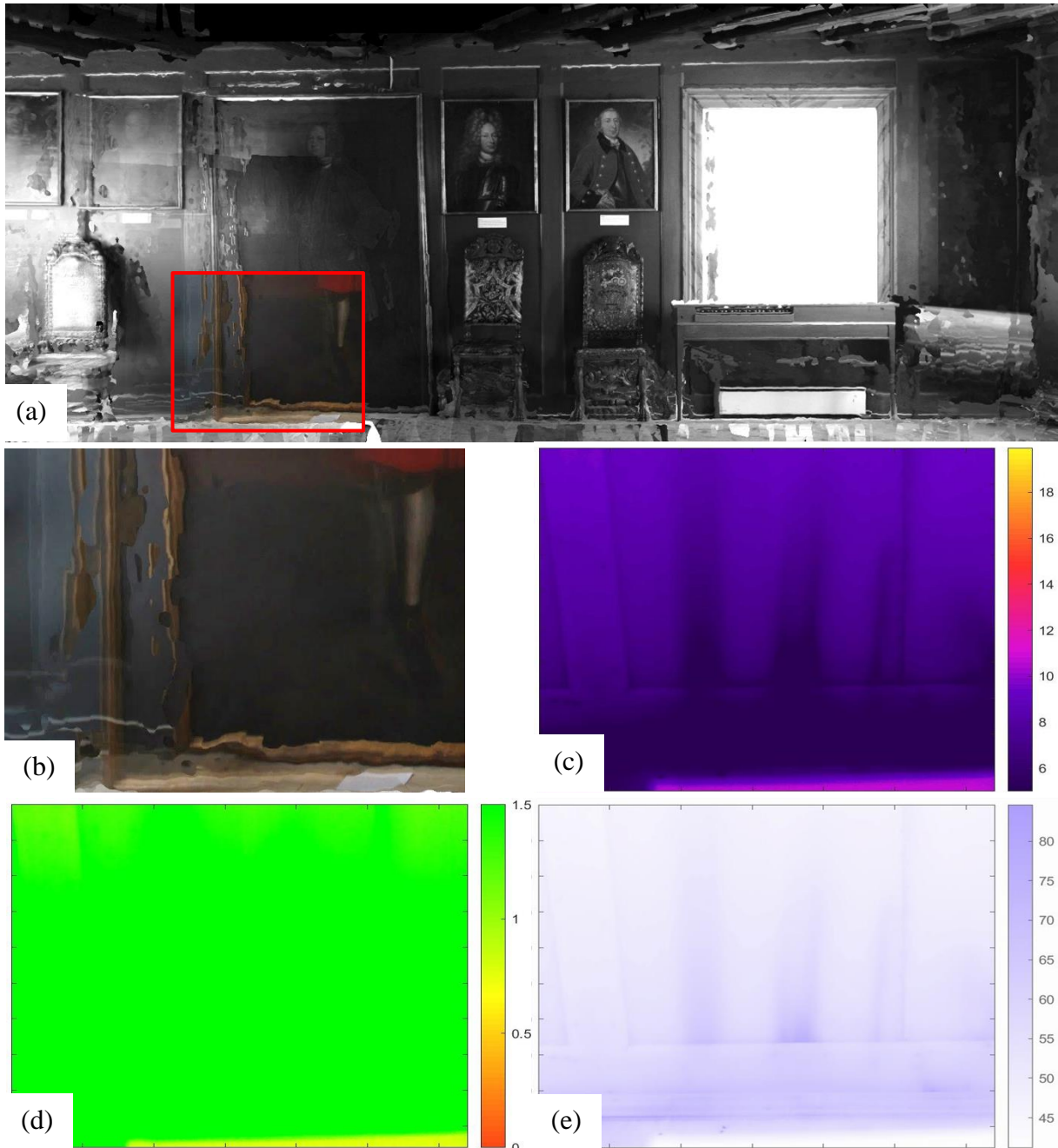

Figure 5.15: (a) is the location and (b) is an orthophoto of a section of the large portrait, while (c) is the surface temperature, (d) is the thermal transmittance and (e) is the relative humidity on the surface of the corresponding area behind the portrait section.

Figure 5.15 (c) displays lower temperatures than what was displayed in figure 5.14 (c), ranging from 5 – 8 °C. The thermal transmittance in figure 5.15 (d) has little to no areas where the values are lower than 1.5 W/m^{2}K. For the relative humidity, figure 5.15 (e), the scale had to have a greater range as the section had higher values of relative humidity than figure 5.14 (e). Most of the wall surface has a relative humidity of around 55 – 60 %, but in some of the lower areas in figure 5.15 (d) have a relative humidity exceeding 80 %.

5.3 Atmospheric measurements

5.3.1 Atmospheric temperature
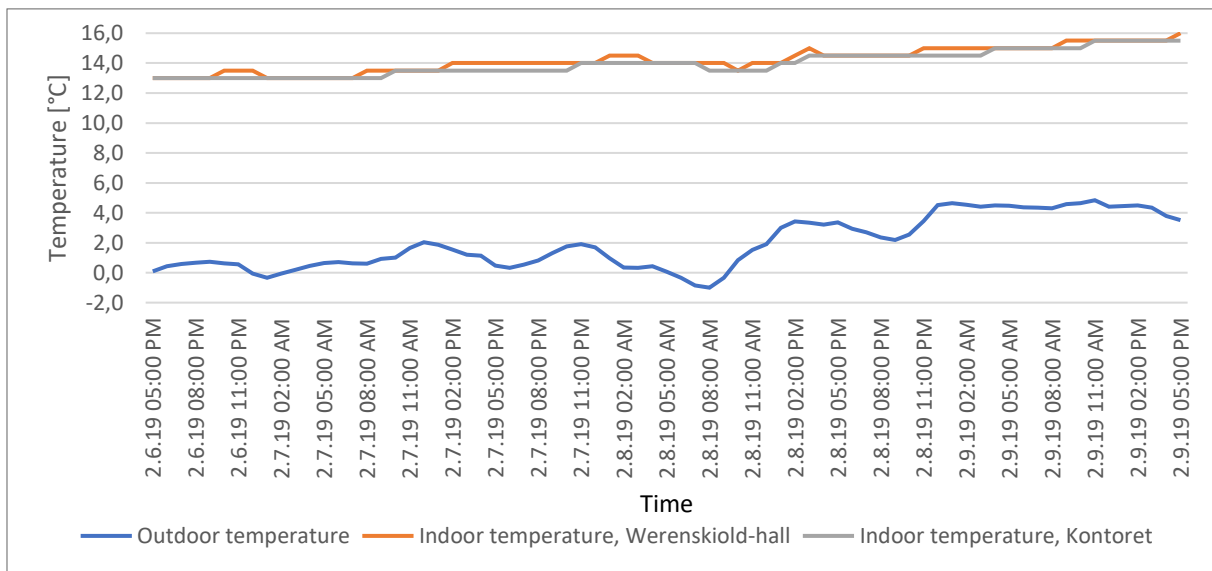
Figure 5.16: Atmospheric temperatures outdoor and indoor.

The indoor measurements of the atmospheric temperature are within the range of 13 – 15 °C for Kontoret and 13 – 15.5 °C for Werenskiold-hall. Kontoret has slightly lower temperatures throughout the measured period than Werenskiold-hall. Overall, the indoor atmospheric temperature did not differ by more than 3 °C over the measured period. For the outdoor temperature, there were measured stronger fluctuations ranging from -1.0 – 4.8 °C.

5.3.2 Atmospheric relative humidity
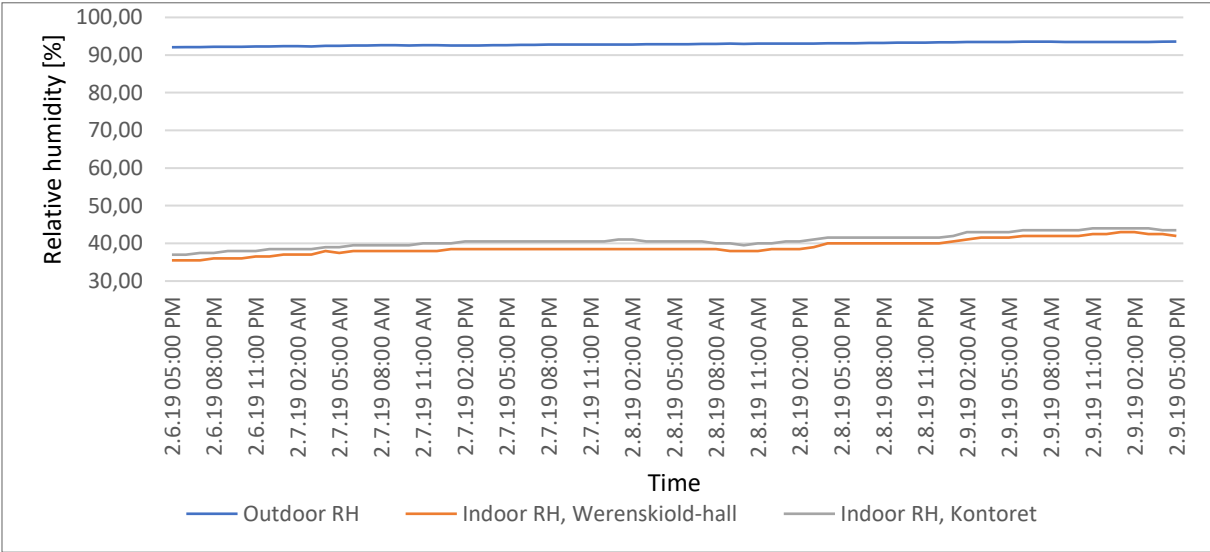
Figure 5.17: Atmospheric relative humidity's outdoor and indoor.

There are little to no fluctuations in relative humidity for both the indoor and outdoor measurements during the measured period. For the indoor measurement, the relative humidity steadily increases from around 35 to 42 %. The relative humidity in Kontoret, is slightly higher than the one for Werenskiold-hall. The outdoor relative humidity is considerably higher than both the indoor measurements, ranging from 92 – 94 %.

5.3.3 Outdoor wind speed
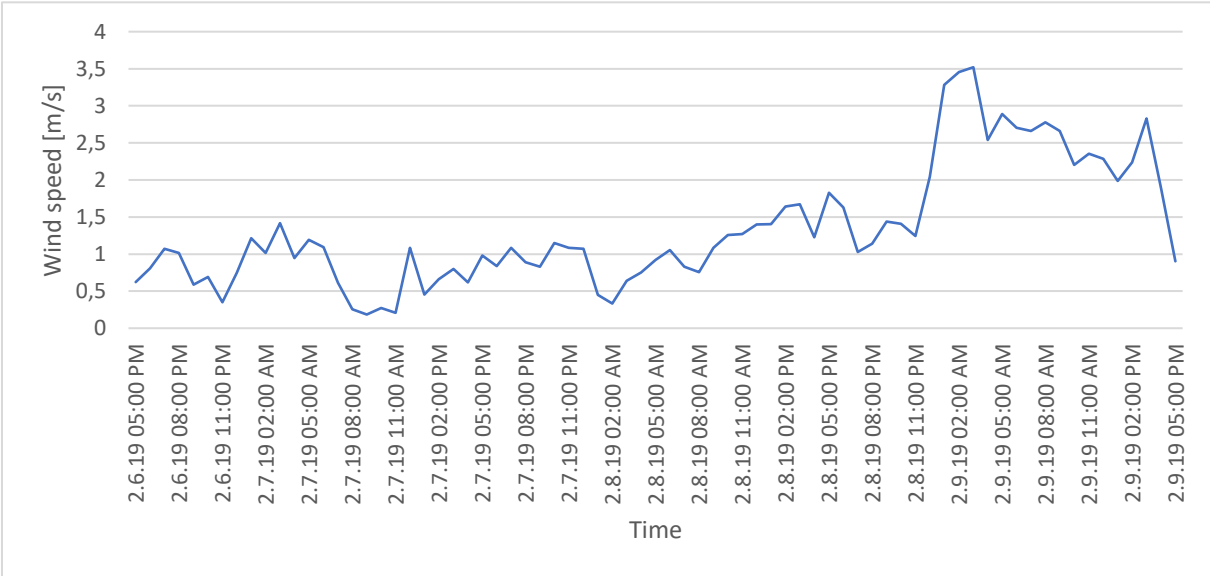
Figure 5.18: Outdoor wind speed.

There were strong fluctuations in the measured wind speed during the measured period, ranging from 0.2 to 3.5 m/s.

5.4 Point measurements

5.4.1 Indoor surface temperature
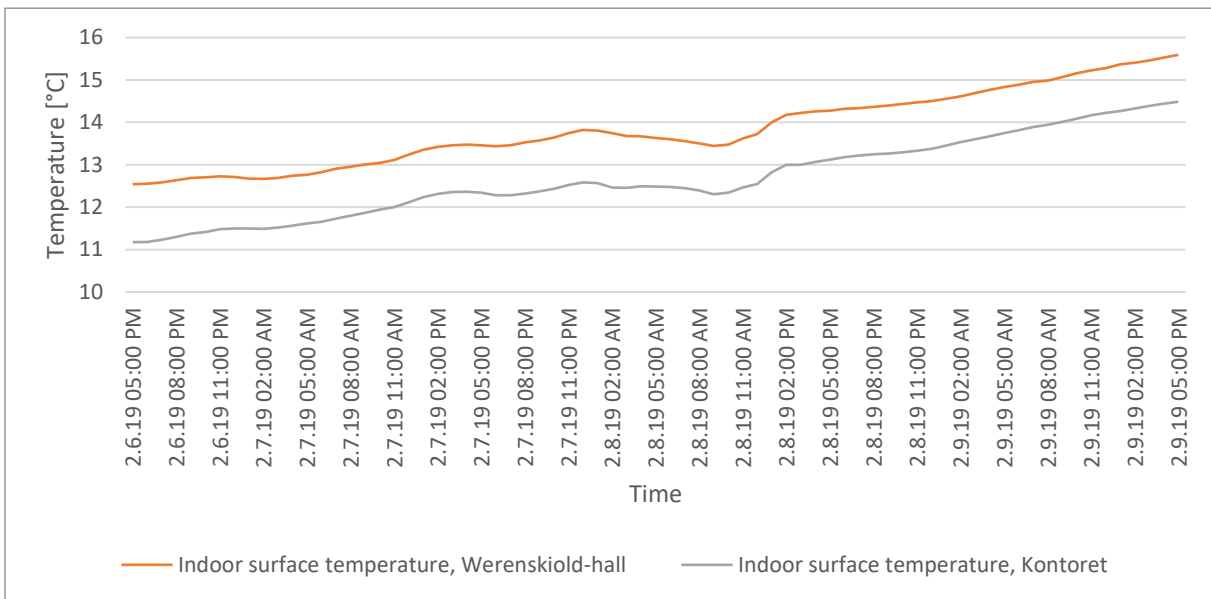
Figure 5.19: Indoor surface temperatures measured with TRSYS01.

Figure 5.19 illustrates the hourly average indoor surface temperature of the measured area in Kontoret and Werenskiold-hall. The temperature sensors have very similar results, only deviating with a slightly lower surface temperature in Kontoret than Werenskiold-hall. In Kontoret, the temperature steadily increases from 11 to 14.5 °C, while the temperature in Werenskiold-hall increased from 12.5 to 15.5 °C. The difference between the two locations is in average 1.2 °C.

5.4.2 Outdoor surface temperature
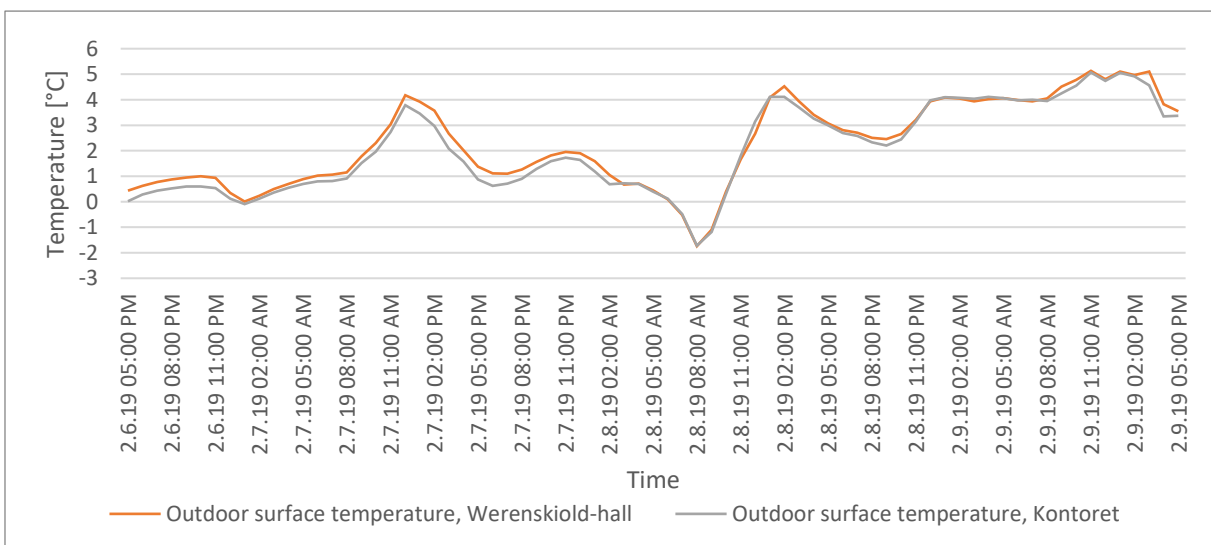
Figure 5.20: Outdoor surface temperatures measured with TRSYS01.

The hourly average outdoor surface temperatures measured are displayed in figure 5.20. There is only a slight deviation in surface temperature between Kontoret and Werenskiold-hall. On average, the surface temperature measured in Kontoret is slightly lower than the measurements in Werenskiold-hall.

5.4.3 Absolute temperature difference
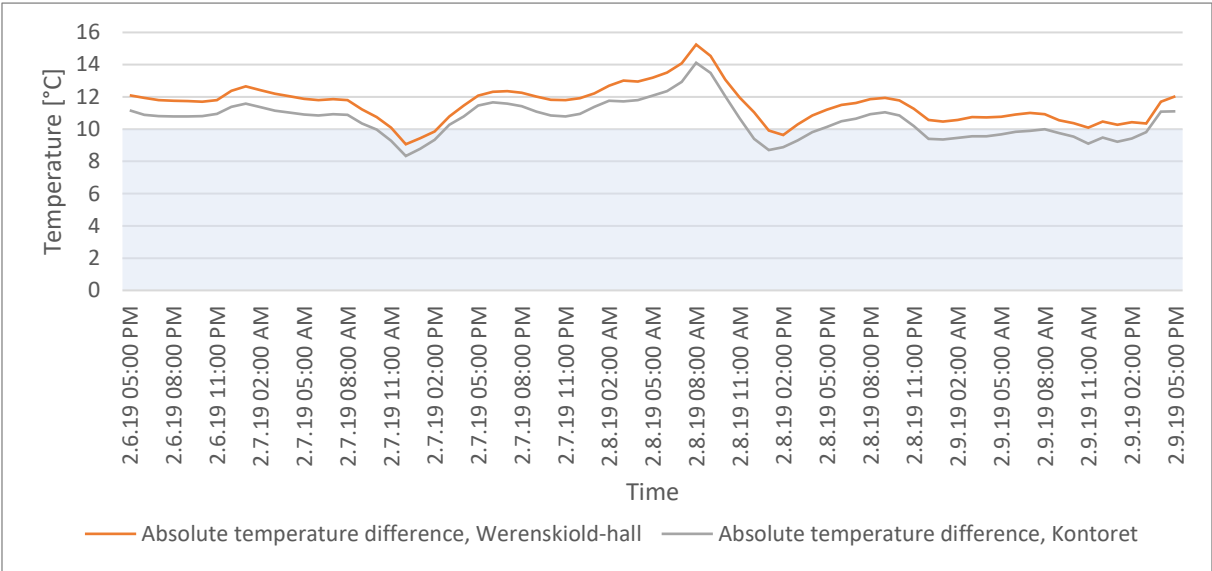
Figure 5.21: Absolute temperature difference between the indoor and outdoor surface temperatures for Kontoret and Werenskiold-hall.

The absolute temperature difference between the indoor and outdoor surface temperature is shown in figure 5.21. Both graphs indicate the absolute temperature difference may drop below 10 °C during the day. During the night, the absolute temperature difference exceeds 10 °C at most times. However, the absolute temperature difference for Kontoret drops occasionally below 10 °C during the last night. Kontoret also has an overall lower absolute temperature difference than Werenskiold-hall.

5.4.4 Average heat flux measurements
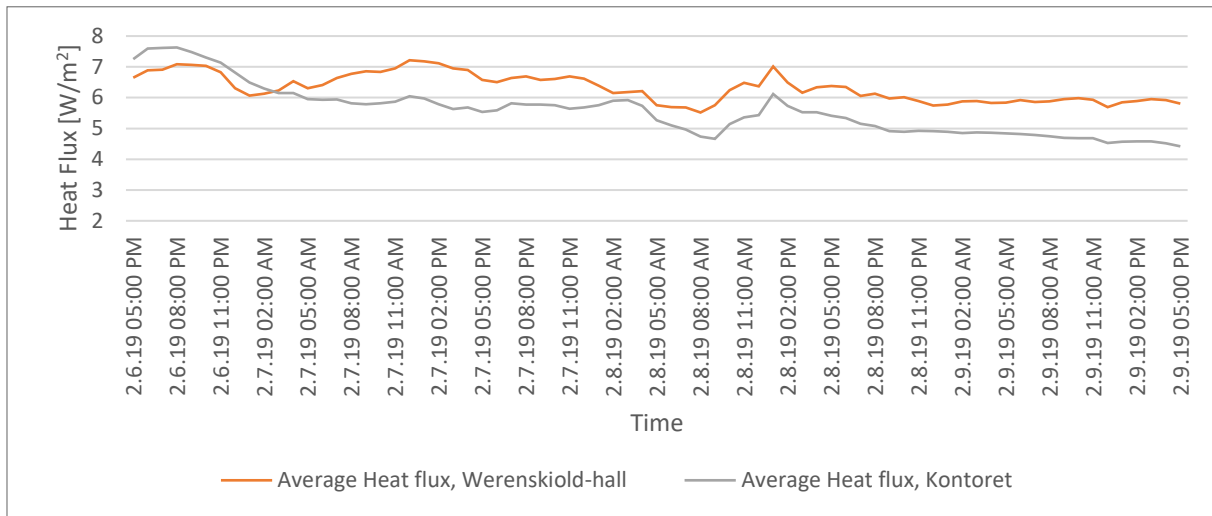
Figure 5.22: Hourly average heat flux for Kotoret and Werenskiold-hall measured with TRSYS01.

Figure 5.22 illustrates the average heat flux measured from the selected exterior walls in Snekkenes. The measurements for Werenskiold-hall are relatively even throughout the measured period, while the measurements for Kontoret decreases over the measured period.

The average heat flux measured in Werenskiold-hall is around $6 - 7$ W/m^2, which is a difference of 1 W/m^2. For Kontoret, the average heat flux decreases from 7.5 to 4.5 W/m^2 throughout the measured period, which is a difference of 3 W/m^2.

5.5 The thermal resistance and thermal transmittance based on the point measurements
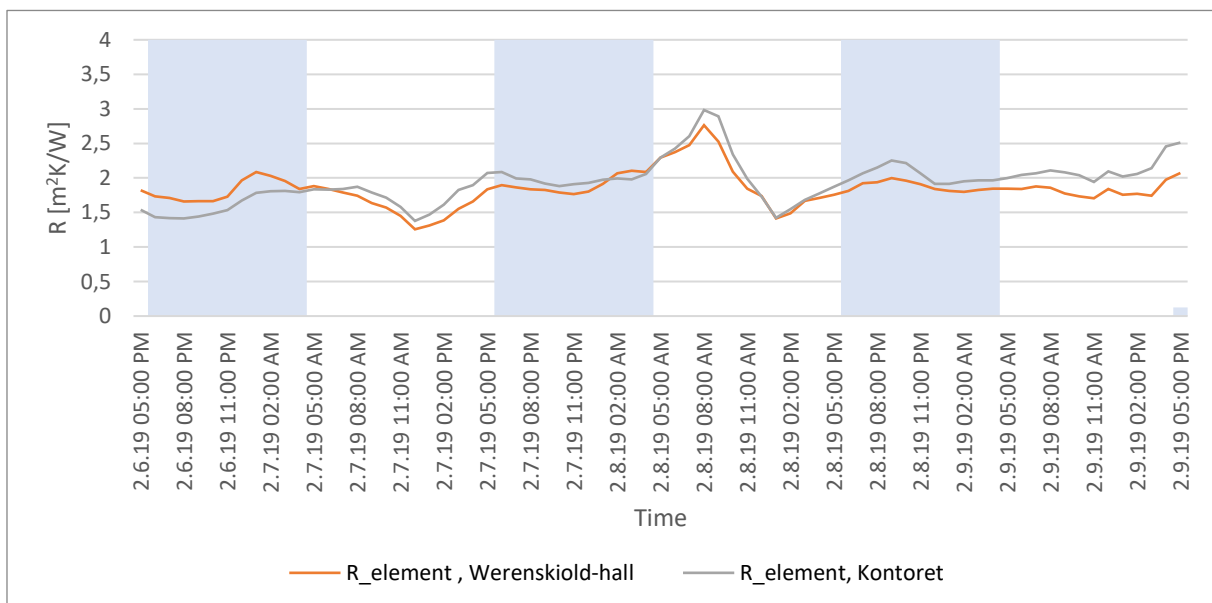
Figure 5.23: Hourly average thermal resistance of the element for Kontoret and Werenskiold-hall.

The hourly average thermal resistance, of the two measured elements, is plotted in figure 5.23. The values from Kontoret are slightly higher at the end of the measured period, while the values from Werenskiold-hall is around 1.8 – 2.2 m^{2}K/W during the three nights. During daytime, the white areas, the measurements fluctuate more and can deviate as much as 1.5 m^{2}K/W. The blue area indicates the values which were further processed in section 5.5.1 and 5.5.2.

5.5.1 Kontoret

Table 5.1: The average thermal resistance of the element for Kontoret.

Period	Average $R_{element}$ [m^{2}K/W]	5% lower limit [m^{2}K/W]	5% upper limit [m^{2}K/W]	Standard deviation [m^{2}K/W]
Day 1: 2.6.19 06:00 PM to 2.7.19 04:00 AM	1.60	1.52	1.68	0.17
Day 2: 2.7.19 06:00 PM to 2.8.19 04:00 AM	1.97	1.87	2.07	0.06
Day 3: 2.8.19 06:00 PM to 2.9.19 04:00 AM	2.04	1.94	2.14	0.12
Total	1.87			0.23

The average thermal resistance from the measurements differed more than 5 % for the three subsequent nights. As the measurements did not correspond to ISO 9869, Kontoret was not further processed.

5.5.2 Werenskiold-hall

Table 5.2: The average thermal resistance of the element for Werenskiold-hall.

Period	Average $R_{element}$ [m^{2}K/W]	5% lower limit [m^{2}K/W]	5% upper limit [m^{2}K/W]	Standard deviation [m^{2}K/W]
Day 1: 2.6.19 06:00 PM to 2.7.19 04:00 AM	1.82	1.73	1.91	0.15
Day 2: 2.7.19 06:00 PM to 2.8.19 04:00 AM	1.90	1.81	2.00	0.12
Day 3: 2.8.19 06:00 PM to 2.9.19 04:00 AM	1.88	1.78	1.97	0.07
Total	1.87			0.12

For Werenskiold-hall, the average thermal resistance from the measurements did not differ more than 5 % for the three subsequent nights. The total average thermal resistance, for wall in Werenskiold-hall, was calculated to be 1.87 m^{2}K/W with a standard deviation of 0.116 m^{2}K/W. From this, the thermal transmittance of Werenskiold-hall was found to be 0.42 ± 0.02 W/m^{2}K, see table 5.3.

Table 5.3: The total thermal resistance and thermal transmittance of the element in Werenskiold-hall.

	R-value [m^{2}K/W]	U-value [W/m^{2}K]
$R_{si} = 1/h_i$	0.41	
$R_{average}$	1.87	0.54
$R_{se} = 1/h_c$	0.10	
Total	2.37	0.42 ± 0.02

5.6 Comparison between the thermal transmittance of the heat flow meter method and thermography
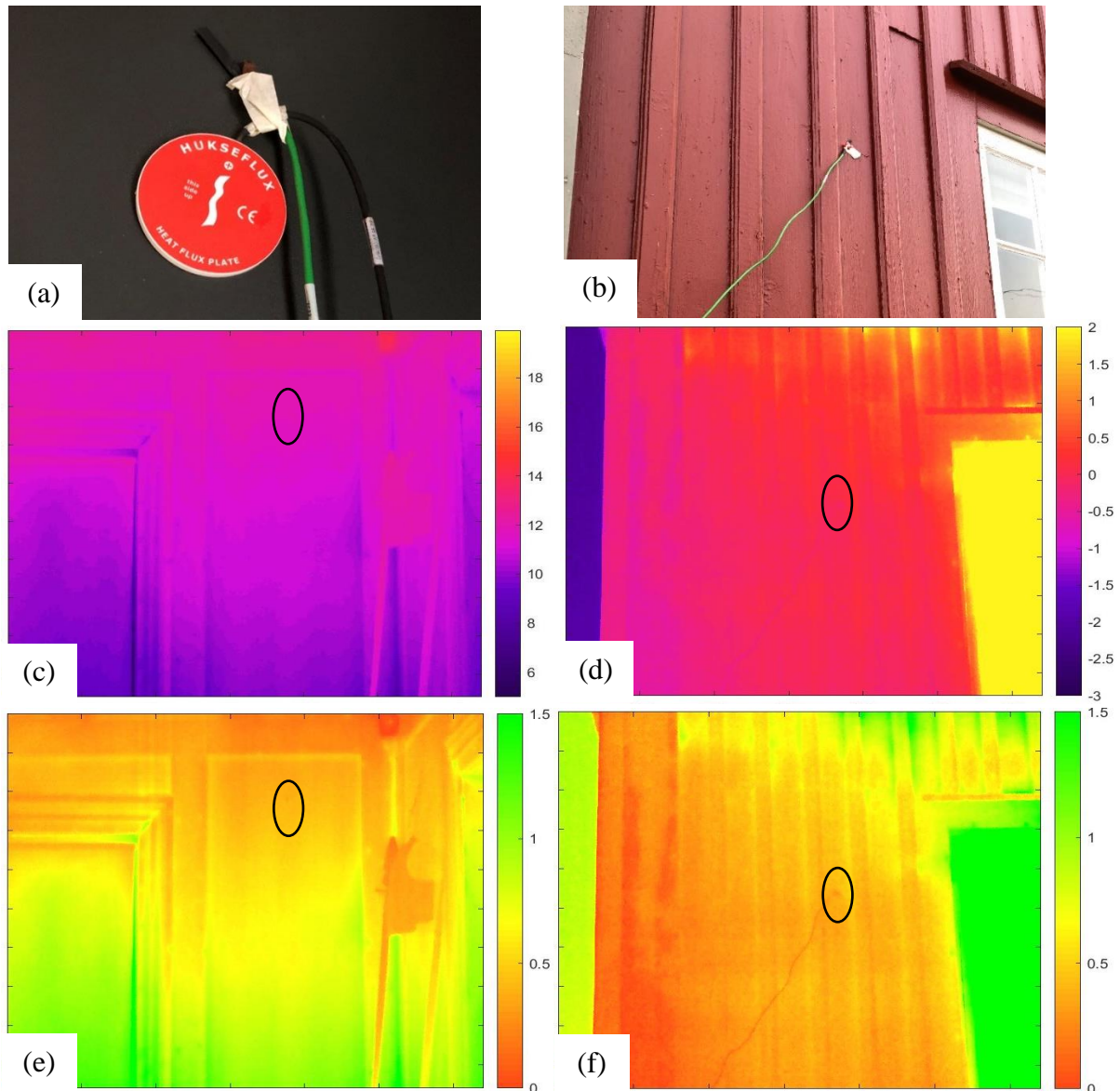
Figure 5.24: The location of the TRSYS01 sensors indoor (a) and outdoor (b), as well as the thermal images indoor (c) and outdoor (d, and the thermal transmittance indoor (e) and outdoor (f).

From the heat flow meter method, the thermal transmittance was found to be 0.42 ± 0.02 W/m^{2}K in Werenskiold-hall. This value was compared with an estimated thermal transmittance based on the construction's composition, which was 0.42 W/m^{2}K, see appendix 9.2. This meant that the measured thermal transmittance, from the measurement with the heat flow, did not differ from the estimated thermal transmittance based on the construction's composition.

The marked area in figure 5.24 is the same area as the TRSYS01 sensors were mounted in Werenskiold-hall. In figure 5.24, the average thermal transmittance, of the marked area, was found to be 0.43 W/m^{2}K indoor and 0.42 W/m^{2}K outdoor. Indoor, the thermal transmittance

differed with only 1 % between the thermal transmittance calculated from the heat flow meter method and the thermal transmittance calculated from the thermographic images. For the outdoor measurements, there was no difference between the resulting thermal transmittance from the heat flow meter method and the thermal transmittance calculated from the thermographic images.

6. Discussion

This chapter discusses the results displayed in chapter 5. Section 6.1 focuses on the point measurements. In section 6.2, the thermal transmittance maps are discussed, while in section 6.3, discussed the maps of the relative humidity on the surfaces. Section 6.4 focuses on misleading errors in the results generated with Pix4D.

6.1 Point measurements

From the results, only the measurements taken at Werenskiold-hall were further processed as the thermal resistance differed by more than 5 % over the three subsequent nights at Kontoret.

There were many factors to be considered when mounting the TRSYS01 sensors to the walls. As the usage of existing nails was required at the mounted location indoor and the outdoor sensor had to be at the same location as the indoor sensors, the sensors may have been exposed to e.g. sun, rain and drafts.

The results show little to no difference between the surface temperatures for the outdoor measurements, while the indoor surface and atmospheric temperature is overall lower in Kontoret than in Werenskiold-hall. This indicates that the sensors at Kontoret may have been influenced by e.g. drafts. In comparison to Werenskiold-hall, Kontoret is closer to the entrance of Snekkenes, which may have affected the measured temperatures.

Because of the lower surface temperature indoor, Kontoret did not meet the required 10 °C temperature difference between the indoor and outdoor measurements. Werenskiold-hall also had times when the absolute temperature difference did not exceed 10 °C, but this was only during daytime. The results also showed an overall decrease in the heat flux measured over the measured period. These conditions may be the cause the thermal resistance in Kontoret differed more than 5 % for the three subsequent nights.

6.2 Mapping of the thermal transmittances

Section 5.6 showed that there were little to no difference between the thermal transmittances based on different calculation methods. Therefore, the method used to retrieve the maps and images of the thermal transmittance were considered correct for this area. This, however, was not the case for other areas of the walls. The thermal transmittance maps and images in section 5.1 and 5.2 indicated variations in the thermal transmittance, both indoor and outdoor.

6.2.1 Comparison between indoor and outdoor index maps

Figure 6.1 display a section of the figure 5.3 (b) and figure 5.9 (b), which shows a clear difference between the indoor and outdoor thermal transmittance maps of the same wall section. As the thermal properties should be consistent of the same area on the wall, both indoor and outdoor, the maps may be influenced by different factors.
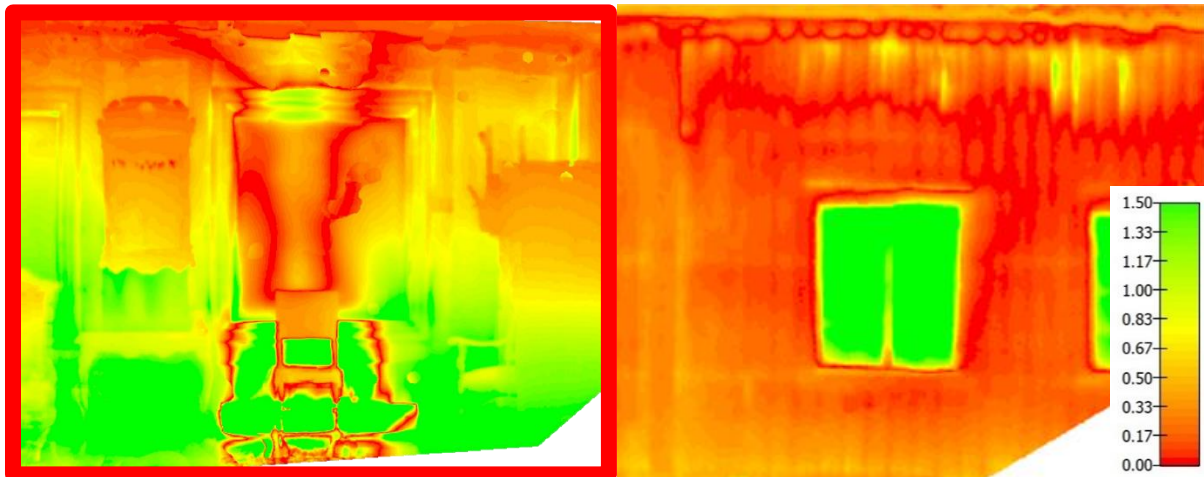

Figure 6.1: Thermal transmittance maps of indoor wall I1 and outdoor wall O2 of the same area.

The results in section 5.1.1 and 5.1.4 also shows that the surface temperature indoor variates more than the more homogenous surface temperatures outdoor. This indicates that the surface temperature may greatly affect the thermal transmittance.

From the indoor maps, section 5.1, convection caused by the electric radiators may be the main source of the variating surface temperatures across the walls. The maps indicate that the areas closer to the ceiling and above the electric radiator are more affected by the convection, as the temperatures in these areas are higher. Behind the removed portraits and in areas closer to the floor, the temperatures were lower indicating that these areas may have been less affected by the convection.

As there may be a great variation in convection across the walls, the internal convective heat transfer coefficient only applies for certain areas. Other areas, such as above the electric radiator or closer to the floor, another internal convective heat transfer coefficient may be necessary in order to display the correct thermal transmittance of the wall. The thermal transmittance maps indoor, of larger areas, may therefore be an inaccurate presentation of the thermal transmittance of the walls. Behind the removed portraits also indicated that these areas may be affected differently by the convection than the other surfaces around. If the convection had been similar over the whole wall, the convection may not have influenced the calculated thermal transmittance indoor to such degrees.

Though the variations in the thermal transmittance maps were greater for the indoor walls, there were also variations in the outdoor maps. As the survey was performed on a cloudy day, the transmittance maps should not have been affected by sun radiation. However, the vegetation around Snekkenes may have influenced the results. In section …, a possible influence on the

thermal transmittance was found to be a tree located not too far from the building. This indicates that other elements, e.g. other buildings, may influence the thermal transmittance in a similar way.

6.2.2 Linear thermal transfer coefficient

Figure 5.12 (b), displayed high values of thermal transmittance in the area between the upper and lower floors, indicating that this thermal transmittance may have been influenced by a thermal bridge caused by the floor junction. This floor junction may also have influenced the thermal transmittance in the areas around it, though they may seem unaffected.

As the linear thermal transmittance was calculated based on the thermal transmittance calculated at the location of the sensors in Werenskiold-hall, it should not have been influenced by the floor junction. However, as the sensors were mounted a distance away from the marked area in section 5.1.5, the two areas may have been affected by different conditions. If one of these areas are affected by a different reflected temperature, this may influence the linear thermal transfer coefficient.

6.3 Mapping of the relative humidity on the surface

Like the thermal transmittance maps, the maps of the relative humidity on the surface may also have been highly influenced by the convection from the electric radiators. The results in section 5.1.1, 5.1.2 and 5.1.3, indicated that areas closer to the ceiling and the electric radiator have lower values of relative humidity than areas closer to the floor. As convection is a form of thermal transfer were the heat rises, the temperatures in the higher areas may have been greater influenced by this form of thermal transfer than the lower areas. On the other hand, if the convection was evenly distributed over the surfaces, the calculated resulting relative humidity on the surfaces may have differed.

The highest levels of relative humidity were found in the lower areas of the walls. As these areas may be affected less by the convection in the room, these areas may be at a higher risk of mold growth than other areas. The relative humidity in these areas did, however, not exceed 75 % and may therefore not be at high risk of mold growth at that moment the thermographic survey was performed. However, if the surface temperature decreases and/or the atmospheric relative humidity increases, these areas may be at higher risk of mold growth than the areas more influenced by the convection.

Figure 5.3 also indicated an interesting result as the area under the mirror had slightly higher values of relative humidity than other areas at the same height. This might be because the mirror itself hinders the convection from the electric radiators in reaching this area. The same might be for other objects which hinders the convections, such as other wall decorations and furniture, indicating that these areas may also be at higher risk of mold growth.

6.3.1 Behind portraits

The results in section 5.2 display higher values of relative humidity behind the portraits than the areas around or areas at the same height. For the smaller portrait, the relative humidity was at its highest in the area where the portrait touched the wall surface. This may be because this area is the least affected by the convection in the room. Although this area does not have a relative humidity above 75 % at that exact moment, an increase in the atmospheric relative humidity and/or a decrease in the surface temperature may give different results. As the relative humidity is higher in this area, it may be exposed to higher levels of relative humidity than the areas around with lower relative humidity. Therefore, this area might have a higher risk of growth than the areas around.

The surfaces behind the larger portrait was a little different from what was found behind the small portrait. In the area higher up, the relative humidity behind the portrait differed only slightly from the areas around. However, closer to the floor, the relative humidity even exceeded 80 % in some areas. The areas behind the larger portrait, especially by the floor, may therefore be more exposed to a higher risk of mold growth than other areas with lower levels of relative humidity. If the atmospheric relative humidity increases and/or the surface temperature decreases, a larger quantity of this area may also have a relative humidity exceeding 75 % and may be at a higher risk of mold growth.

6.4 The results generated from Pix4D

The processing in Pix4D may have generated errors in the generated maps and orthophoto. Figure 6.2 displays some of the possible errors that may give misleading results. The error that might be the most significant is the furniture which appears as transparent figures. As many of these are a bit diffuse, they may not be seen as actual objects and instead be analyzed as part of the wall surface. There may also be an uncertainty in the thermal maps, caused by the inhomogeneity in the direction of the emitted radiation, as the thermal images were taken from different angles.
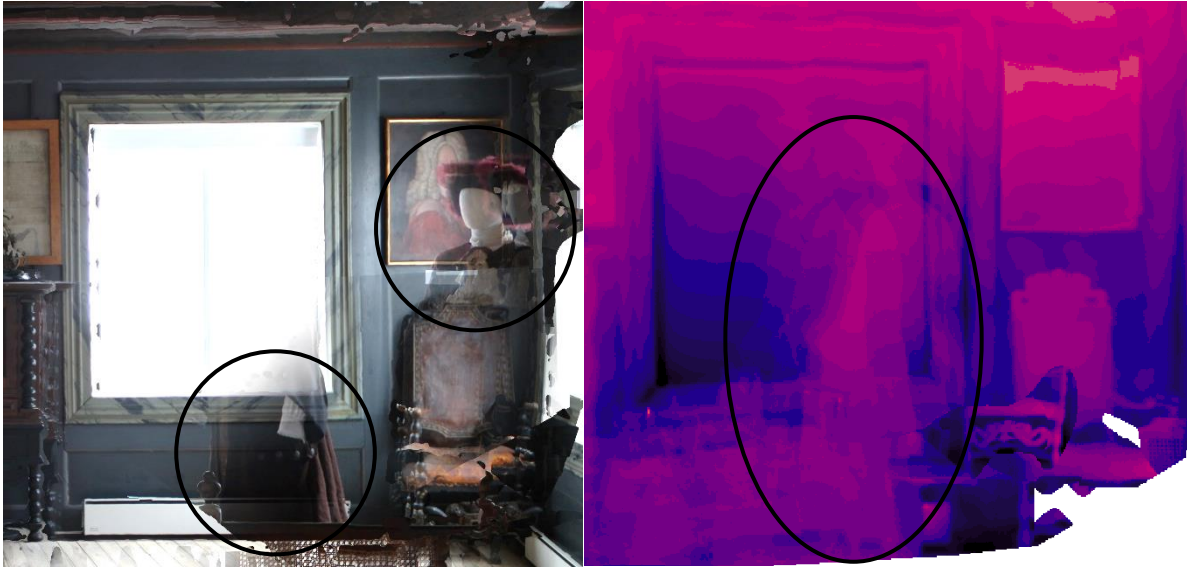
Figure 6.2: Possible errors in the othophotos (left) and maps (right).

7.Conclusion

The presented thesis mapped the thermal transmittance and surface moisture of walls for the historical building Snekkenes at Borgarsyssel Museum, with the use of thermography and heat flow meters.

The indoor mapping showed that the results are affected by thermal convection in the room. The mapping of the relative humidity on the surfaces indicated areas where the calculated relative humidity was higher than other areas. This was especially the case in areas behind the portraits, closer to the floor and where objects hindered the convection in general, e.g. furniture and wall decorations. As these areas have a higher value of relative humidity, they are more likely to be at risk of mold growth than areas where the relative humidity on the surface was lower. In order to decrease the risk of mold growth in these areas, forced convection may be a possible solution.

The mapping of the thermal transmittance was also affected by convection, resulting in strong variations in the calculated thermal transmittance of the walls, also behind the removed portraits. As the different areas were affected differently by the convection, the internal convective heat transfer coefficient selected in this thesis only applied for certain areas of the wall surface.

Outdoor, the reflected temperature between wall sections and other elements, such as trees, influenced the calculated thermal transmittance in the maps. There is therefore also an uncertainty in the calculation of the linear thermal transmittance if the U_{TB} and U_o are affected by different reflected temperatures. However, if the U_{TB} and U_o are affected by the same conditions, such as the same reflected temperature, the results should give reliable results.

7.1 Further research

The results of this thesis indicate that further research is necessary in order to achieve a better mapping of the walls. For the indoor thermal transmittance, forced convection could possibly give a better estimate of the wall's thermal transmittance. A step further would also be to generate 3D BIMs of the wall's thermal transmittance and relative humidity on the surfaces. It might then be necessary to have a professional do the processing of the photogrammetry in order to achieve acceptable 3D models.

8. Bibliography

Andersen, Ø. (1981). *Fotogrammetri grunnkurs*. nlh: NLH.

Ankersmit, B. & Stappers, M. H. L. (2017). *Managing Indoor Climate Risks in Museums*. Cham: Springer International Publishing : Imprint: Springer.

Bienvenido-Huertas, D., Bermúdez, J., Moyano, J. J. & Marín, D. (2019). Influence of ICHTC correlations on the thermal characterization of façades using the quantitative internal infrared thermography method. *Building and Environment*, 149: 512-525. doi: 10.1016/j.buildenv.2018.12.056.

Bolton, D. (1980). The computation of equivalent potential temperature. *Monthly Weather Review*, 180: 1046-1053.

Borgarsyssel museum. Available at: https://www.visitoestfold.com/no/sarpsborg/Artikler/Borgarsyssel-museum/ (accessed: April 5, 2019).

Borgarsyssel Museum. (2016). *Rapport: Befaring Borgarsyssel 04.05.16 - muggfjerning Snekkenes 16.06.2016*.

Butcher, G. (2016). Infrared Waves. In Parkinson, C. L. & Wollack, E. J. (eds) *Tour of the Electomagnetic Spectrum*, pp. 14-15. Washington, DC: National Aeronautics and Space Administration, . Available at: https://smd-prod.s3.amazonaws.com/science-pink/s3fs-public/atoms/files/Tour-of-the-EMS-TAGGED-v7_0.pdf (accessed: March 26, 2019).

Çengel, Y. A., Ghajar, A. J. & Kanoğlu, M. (2015). *Heat and mass transfer : fundamentals and applications*. 5th ed. in SI units. ed. New York, NY: McGraw-Hill Education.

Dick, Ø. B. (2003). *Geomatikk - kartfaglig bildebruk*. 1 ed. Oslo: Gan.

Edvardsen, K. I. & Ramstad, T. Ø. (2014a). Klima. In *Håndbok 5 Trehus*, pp. 381-384. Oslo: SINTEF akademisk forlag.

Edvardsen, K. I. & Ramstad, T. Ø. (2014b). Varme. In *Håndbok 5 Trehus*, pp. 388-401. Oslo: SINTEF akademisk forlag.

emissivitet. (2018). Store norske leksikon. Available at: https://snl.no/emissivitet (accessed: March 15, 2019).

Environment, M. *4-IN-1 SENSOR TEMP/RH/BAROMETRIC PRESSURE/VAPOR PRESSURE*. Available at: https://www.metergroup.com/environment/products/atmos-14/ (accessed: April 5, 2019).

FLIR. *FLIR Tools*. Available at: https://www.flir.com/products/flir-tools/ (accessed: March 15, 2019).

FLIR. (2014). *User's manual* FLIR T6xx series. Wilsonville, USA. Available at: https://www.ivytools.com/v/flir-manuals/t6xx-series/flir-t640-manual.pdf (accessed: February 20, 2019).

Folkehelseinstituttet. (2013). Råd for å unngå fukt og mugg. Available at: https://www.fhi.no/ml/miljo/inneklima/fremhevede-artikler-inneklima-og-helse/fuktproblemer-og-muggvekst-i-bygnin/#vekstbetingelser-for-muggsopp- (accessed: March 23, 2019).

Garrido, I., Lagüela, S. & Arias, P. (2018). Autonomous thermography: towards the automatic detection and classification of building pathologies. Available at: https://www.researchgate.net/publication/326112389_Autonomous_thermography_towards_the_automatic_detection_and_classification_of_building_pathologies (accessed: April 20, 2019).

Gustavsen, A., Thue, J. V., Blom, P., Dalehaug, A., Aurlien, T., Grynning, S. & Uvsløkk, S. (2008). Kuldebroer – Beregning, kuldebroverdier og innvirkning på energibruk. 25. Available at: https://www.sintef.no/globalassets/upload/byggforsk/publikasjoner/sb_prosjektrapport_25.pdf (accessed: February 20, 2019).

Haga, I. (2019). *Optimalisering av inneklima og energiforbruket i halvklimatiserte museumsbygninger*. Unpublished manuscript.

Holme, J. & Geving, S. Unngå byggskader: Reduser risikoen for mugg- og råtesopp. *ByggAktuelt*, 3 (10). Available at: https://www.sintef.no/globalassets/upload/artikkel-03-10-byggaktuelt.pdf (accessed: March 6, 2019).

Huijbregts, Z., Kramer, R. P., Martens, M. H. J., Schijndel, v. A. W. M., Schellen, H. L. & Building, P. (2012). A proposed method to assess the damage risk of future climate change to museum objects in historic buildings. *Building and Environment*, 55 (sept): 43-56.

Hukseflux. *USER MANUAL TRSYS01* High-accuracy building thermal resistance measuring system with two measurement locations (accessed: January 10, 2019).

International Organization for Standardization. (2014). *ISO 9869: Thermal insulation - Building elements - In-situ measurement of thermal resistance and thermal transmittance*. Part 1: Heat flow meter method. Geneve: ISO (accessed: April 5, 2019).

Jayamaha, S. E. G., Wijeysundera, N. E. & Chou, S. K. (1996). Measurement of the heat transfer coefficient for walls. *Building and Environment*, 31 (5): 399-407. doi: 10.1016/0360-1323(96)00014-5.

Jensen, I. Snekkenes. In *Borgarsyssel museum*, pp. 13-20: Østfold Kulturminnevern.

Kemp, K. K. (2008). Photogrammetry. In *Encyclopedia of Geographic Information Science*, pp. 340-342. Thousand Oaks: SAGE Publications, Inc. Available at: http://search.ebscohost.com/login.aspx?direct=true&db=nlebk&AN=474337&site=ehost-live (accessed: March 25, 2019).

Kuenzer, C. & Dech, S. (2013). *Thermal Infrared Remote Sensing : Sensors, Methods, Applications*, vol. 17. Dordrecht: Springer Netherlands : Imprint: Springer.

Lawrence, M. G. (2005). The relationship between relative humidity and the dewpoint temperature in moist air: a simple conversion and applications. *Bulletin of American Meteorological Society*, 86 (2): 225. Available at: https://journals.ametsoc.org/doi/pdf/10.1175/BAMS-86-2-225 (accessed: February 26, 2019).

Madding, R. (2008). Finding R-values of Stud-Frame Constructed Houses with IR Thermography. *Information 2008*, 9: 261-277. Available at: https://www.researchgate.net/publication/285737245_Finding_R-values_of_Stud-Frame_Constructed_Houses_with_IR_Thermography (accessed: April 15, 2019).

Metningstrykk. (2009). Store norske leksikon. Available at: https://snl.no/metningstrykk (accessed: March 8, 2019).

Monteith, J. L. & Unsworth, M. H. (2013). Dew-Point Temperature. In *Principles of environmental physics : plants, animals, and the atmosphere*, p. 13. Oxford, England: Academic Press.

Nardi, I., Sfarra, S. & Ambrosini, D. (2014). Quantitative thermography for the estimation of the U-value: State of the art and a case study. *Journal of Physics Conference Series*, 547: 1-8.

Natephra, W., Motamedi, A., Yabuki, N. & Fukuda, T. (2017). Integrating 4D thermal information with BIM for building envelope thermal performance analysis and thermal comfort evaluation in naturally ventilated environments. *Building and Environment*, 124: 194-208. doi: 10.1016/j.buildenv.2017.08.004.

Pix4D. *Image acquisition*. Available at: https://support.pix4d.com/hc/en-us/articles/115002471546-Image-acquisition (accessed: January 18, 2019).

Pix4D. *Photo stitching vs orthomosaic generation*. Available at: https://support.pix4d.com/hc/en-us/articles/202558869-Photo-stitching-vs-orthomosaic-generation (accessed: March 18, 2019).

Pix4D. *Processing steps*. Available at: https://support.pix4d.com/hc/en-us/articles/115002495706-Processing-steps (accessed: March 7, 2019).

Pix4D. *Processing thermal images*. Available at: https://support.pix4d.com/hc/en-us/articles/360000173463-Processing-thermal-images#label1 (accessed: March 17, 2019).

Pix4D. (2017a). *Indoor mapping game plan*. Available at: https://www.pix4d.com/blog/indoor-mapping-game-plan (accessed: January 25, 2019).

Pix4D. (2017b). *Pix4Dmapper 4.1 User Manual*. Lausanne, Switzerland. Available at: https://support.pix4d.com/hc/en-us/articles/204272989-Offline-Getting-Started-and-Manual-pdf- (accessed: March 15, 2019).

Quang Huy, T., Dongyeob, H., Choonghyun, K., Achintya, H. & Jungwon, H. (2017). Effects of Ambient Temperature and Relative Humidity on Subsurface Defect Detection in Concrete Structures by Active Thermal Imaging. *Sensors*, 17 (8): 1718. doi: 10.3390/s17081718.

SINTEF Byggforsk. (1999). *471.016 Kuldebroer. Metoder for å bestemme kuldebroverdi* (accessed: February 20, 2019).

SINTEF Byggforsk. (2008). *Kuldebroer. Konsekvenser og dokumentasjon av energibehov* (accessed: February 20, 2019).

Termografi: avbilding. (2018). Store norske leksikon. Available at: https://snl.no/termografi_-_avbildning (accessed: March 6, 2019).

Thiis, T. K., Burud, I., Flø, A. S., Kraniotis, D., Charisi, S. & Stefansson, P. (2017). Monitoring and simulation of diurnal surface conditions of a wooden facade.

Thomas, L., Stuart, R., Stephen, K. & Jan, B. (2013). *Close-Range Photogrammetry and 3D Imaging*. 2nd edition. ed. De Gruyter textbook.: Walter De Gruyter.

Usamentiaga, R., Venegas, P., Guerediaga, J., Vega, L., Molleda, J. & Bulnes, F. G. (2014). Infrared thermography for temperature measurement and non-destructive testing. *Sensors (Basel, Switzerland)*, 14 (7): 12305. doi: 10.3390/s140712305.

Vollmer, M. & Möllmann, K.-P. (2011). Infrared Thermal Imaging. Fundamentals, Research and Applications. . *Physik in unserer Zeit*, 42 (3): 151-151. doi: 10.1002/piuz.201190028.

9. Appendix

9.1 Linear thermal transfer coefficient

Linear thermal transfer coefficient calculations for the thermal bridge caused by the floor junction between the first and second floor.

Average U_o	0.42
Average U_TB	0.89
Width of the floor junction	0.2
Linear thermal transfer coefficient	0.094

9.2 Thermal transmittance estimated with IDA ICE
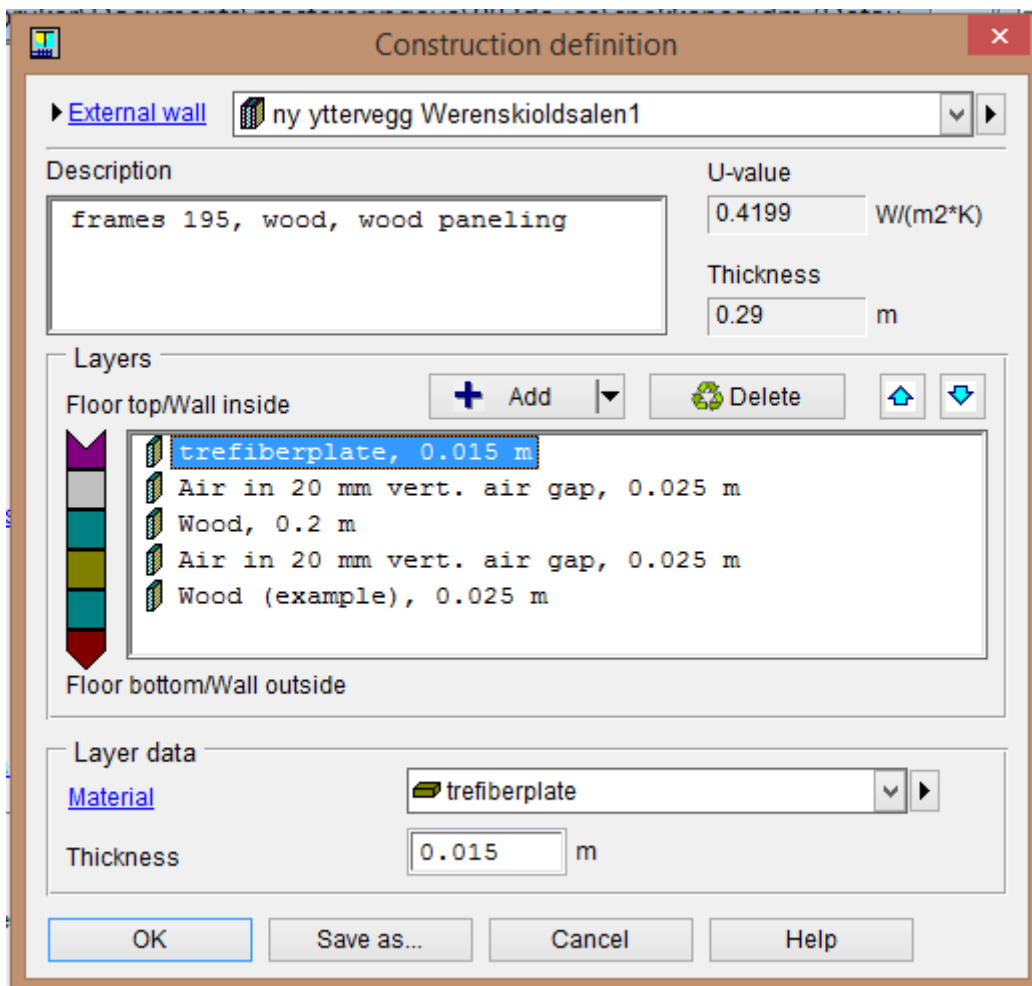
Made by master student Ines Haga (Haga, 2019).

9.3 MATLAB script

9.3.1 Indoor

```matlab
csvfiles = dir('*.csv');
numfiles = length(csvfiles);
results = cell(length(csvfiles),1);
load ('RHCol.mat');
load('UColorRdYlGn.mat');
load('Therm.mat');

% February 6 02:00 PM
%Values for the thermographic survey indoor
Ti = 13.5;      %Atmospheric temp indoor
To = -1.5;      %Atmospheric temp outdoor
RHRom = 34.5;   %Atmospheric RH indoor
RHOut = 91;     %Atmospheric RH outdoor

%October 13 06:00 AM
%Extrem relative humidity, same indoor temperature October 13 12:00 PM
Tie = 13.5;     %Atmospheric temp indoor
Toe = 16.3;     %Atmospheric temp outdoor
RHeRom = 80.5; %Atmospheric RH indoor
RHeOut = 77;    %Atmospheric RH outdoor

%Constants
e = 0.95; % Wall emissivity
Bol = 5.67*10^(-8); %Stefan-Boltzmann constant[W/(m^2K^4)]
A = 17.67;
B = 243.5;

%%RH and U-value
for k = 1:numfiles
    results{k} = xlsread(csvfiles(k).name);
    Td = (B*(log(RHRom/100)+((A*Ti)/(B+Ti))))/(A-log(RHRom/100)-((A*Ti)/(B+Ti)));
    Tde = (B*(log(RHeRom/100)+((A*Tie)/(B+Tie))))/(A-log(RHeRom/100)-((A*Tie)/(B+Tie)));
    x = results{k};

    for i = 1:480
        for j = 1:640
            %Relative humidity on surface
            RH(i,j) = (max(min(100*(exp((17.67*Td)/(243.5+Td))/exp((17.67*x(i,j))/(243.5+x(i,j)))),100),0));
            RHe(i,j) = (max(min(100*(exp((17.67*Tde)/(243.5+Tde))/exp((17.67*x(i,j))/(243.5+x(i,j)))),100),0));
            %Thermal transmittance
            hi = 3.08*(abs(x(i,j)-Ti))^0.25;
            U(i,j) = ((hi*abs(x(i,j)-Ti))+(4*e*Bol*(x(i,j))^3*(x(i,j)-Ti)))/(Ti-To);

        end
```

```matlab
47 -            end
48     %February 6
49 -            climsTherm = [5,19.9];
50 -            t = imagesc(x,climsTherm);
51             %load('RHFarger.mat')
52 -            colormap(Therm), colorbar;
53 -            saveas(t,sprintf('FigureTherm%d.jpg',k));
54
55 -            clims = [0,100];
56 -            h = imagesc(RH, clims);
57             %load('RHFarger.mat')
58 -            colormap(RHCol), colorbar;
59 -            saveas(h,sprintf('FigureRHscale%d.jpg',k));
60
61 -            clims2090 = [30,60];
62 -            hn = imagesc(RH, clims2090);
63             %load('RHFarger.mat')
64 -            colormap(RHCol), colorbar;
65 -            saveas(hn,sprintf('FigureRHscaleNarrow%d.jpg',k));
66
67 -            hh = imagesc(RH);
68             %load('RHFarger.mat')
69 -            colormap(RHCol), colorbar;
70 -            saveas(hh,sprintf('FigureRH%d.jpg',k));
71     %Extreme
72     %    clims = [0,100];
73 -            he = imagesc(RHe, clims);
74             %load('RHFarger.mat')
75 -            colormap(RHCol), colorbar;
76 -            saveas(he,sprintf('FigureRHescale%d.jpg',k));
77
78 -            clims75100 = [75,100];
79 -            hne = imagesc(RHe, clims75100);
80             %load('RHFarger.mat')
81 -            colormap(RHCol), colorbar;
82 -            saveas(hne,sprintf('FigureRHescaleNarrow%d.jpg',k));
83
84 -            hhe = imagesc(RHe);
85             %load('RHFarger.mat')
86 -            colormap(RHCol), colorbar;
87 -            saveas(hhe,sprintf('FigureRHe%d.jpg',k));
88
89             %u = imagesc(U, ...)
90 -            climsU = [0,1.5]
91 -            uu = imagesc(U, climsU);
92 -            colormap(UColorRdYlGn), colorbar;
93 -            saveas(uu,sprintf('FigureU%d.jpg',k));
94
95 -    end
```

9.3.2 Outdoor

```matlab
 3    csvfiles = dir('*.csv');
 4    numfiles = length(csvfiles);
 5    results = cell(length(csvfiles),1);
 6    load('UColorRdYlGn.mat');
 7    load('Therm.mat');
 8
 9    % February 6 03:00 PM
10    %Values for the thermographic survey indoor
11    Ti = 13.5;       %Atmospheric temp indoor
12    To = -0.6;       %Atmospheric temp outdoor
13    v = 0.73;        %Vindspeed [m/s]
14
15    %Constants
16    e = 0.95;             %Wall emissivity
17    Bol = 5.67*10^(-8); %Stefan-Boltzmann constant[W/(m^2K^4)]
18    A = 17.67;
19    B = 243.5;
20
21    %%Calculating U-value and transforming each value into a pixel in the images
22    for k = 1:numfiles
23        results{k} = xlsread(csvfiles(k).name);
24        x = results{k};
25        for i = 1:480
26            for j = 1:640
27                %Thermal transmittance
28                hc = 5.7 + 3.8*v;
29                U(i,j) = ((hc*abs(x(i,j)-To))+(4*e*Bol*(x(i,j))^3*(x(i,j)-To)))/(Ti-To);
30            end
31        end
32    %February 6
33        climsTherm = [-3,2];
34        t = imagesc(x,climsTherm);
35        %load('RHFarger.mat')
36        colormap(Therm), colorbar;
37        saveas(t,sprintf('FigureTherm%d.jpg',k));
38
39      %u = imagesc(U, ...)
40        climsU = [0,1.5];
41        uu = imagesc(U,climsU);
42        colormap(UColorRdYlGn), colorbar;
43        saveas(uu,sprintf('FigureU%d.jpg',k));
44
45    end
```